CO$_2$ hydrogenation to methanol on intermetallic PdGa and PdIn catalysts and the effect of Zn co-deposition

Naomi Lawes, Nicholas F. Dummer, Samantha Fagan, Oskar Wielgosz, Isla E. Gow, Louise R. Smith, Thomas J.A. Slater, Thomas E. Davies, Kieran J. Aggett, David J. Morgan, Stuart H. Taylor, Graham J. Hutchings, Michael Bowker [*]

Funcat Max Planck Centre for the Fundamentals of Heterogeneous Catalysis, Cardiff Catalysis Institute, Cardiff University, Maindy Road, Cardiff CF24 4HQ, United Kingdom

ARTICLE INFO

ABSTRACT

The behaviour of Pd deposited on Ga$_2$O$_3$ and In$_2$O$_3$ by CVI is compared for the hydrogenation of CO$_2$ to methanol. Ga$_2$O$_3$ alone is inactive, but In$_2$O$_3$ has good conversion, and selectivity as high as 89 % to CH$_3$OH. The addition of Pd to the catalysts had relatively little effect for In$_2$O$_3$, but in contrast, the addition of Pd to Ga$_2$O$_3$, has a very big effect, inducing high activity and selectivity to methanol. Both oxides form Pd intermetallics - Pd$_2$In$_3$ and Pd$_2$Ga. However, for the In catalysts there is also a thick (~3 nm) overlayer of the oxide, while for the Ga catalyst there was no such overlayer. Hence this is why addition of Pd to the Indium catalysts has relatively little effect on performance compared with Ga. Furthermore, the effect of Pd and Zn co-deposition on Ga$_2$O$_3$ and In$_2$O$_3$ was investigated, as well as the effect of the support morphology. Upon co-deposition of Pd and Zn, and after reduction, the Pd$_2$In$_3$ catalyst remains phase stable, whereas the Pd$_2$Ga alloy is replaced by PdZn, and is improved in methanol yield.

1. Introduction

Reducible metal oxide supports are attractive in catalysis due to their ability to carry out catalytic reactions in their own right (for instance Fe$_2$(MoO$_4$)$_3$ for methanol selective oxidation [1,2]), they can influence the properties of metal nanoparticles deposited on them (for instance, changing the charge state of Au [3,4]) or they can form alloys with them [5,6]. In$_2$O$_3$ has gained interest in catalysis, and the formation of In-based alloys, such as Pd-In, have shown promise as bimetallic catalysts for CO$_2$ conversion. Alloying can tune the surface electronic properties, encourage CO$_2$ adsorption, and increase selectivity to methanol [7–10] Aside from the traditional heterogeneous catalysts which are often a metal-supported materials, In$_2$O$_3$ displays unique properties without any metal promoters/co-catalysts. It has emerged as a selective catalyst for CO$_2$ hydrogenation, since it seems that surface oxygen vacancies play a critical role in CO$_2$ activity, can aid in hydrogen activation, and can stabilise the key formate intermediate for methanol synthesis. In-depth studies of the active sites and mechanism are still somewhat limited, however DFT calculations on In$_2$O$_3$ are often a complementary approach to experimental data and aid in the

understanding of adsorption and the activation of CO$_2$ [11–13]. Several studies and reviews have offered insights into CO$_2$ hydrogenation using In$_2$O$_3$ and its selectivity towards methanol, its stability, and the mechanism of the reaction [14–18].

There are three crystal structures for In$_2$O$_3$: cubic bixbyite (c-In$_2$O$_3$), hexagonal corundum (h-In$_2$O$_3$) and orthorhombic (o-In$_2$O$_3$) [19]. Wang et al. reported that c-In$_2$O$_3$ exhibited a higher rate for the reverse water gas shift (RWGS) reaction than h-In$_2$O$_3$, indicating the important role of the crystal phase during the reaction [20]. The authors attributed this to increased CO$_2$ and H$_2$ activation due to the formation of oxygen vacancies on the surface of c-In$_2$O$_3$. For methanol selectivity, Dang et al. suggested that h-In$_2$O$_3$ could exhibit the highest activity and methanol selectivity due to a high proportion of exposed (104) surfaces [21]. Bielz et al. reported that for In$_2$O$_3$ in a reductive environment, the formation of oxygen vacancies led to high CO$_2$ selectivity for the methanol steam reforming reaction (MSR) [22]. Several DFT studies have shown that In$_2$O$_3$ is active for CO$_2$ hydrogenation to methanol and that the activation energy for methanol synthesis is lower than that for the RWGS reaction [23,24]. High activity was also attributed to the cyclic formation and annihilation of oxygen vacancies. Martin et al. showed that

improved activity for CO_2 hydrogenation to methanol could be obtained by incorporating ZrO_2 with In_2O_3 [25]. The study further highlighted that oxygen vacancies can act as active sites and were responsible for excellent catalytic performance. Methanol selectivity reached 100 % at 300 °C and 50 bar. The number of active sites was increased by adding CO to the gas feed, and electronic interactions from ZrO_2 contributed to excellent stability of over 1000 h on stream [25].

Incorporating metals such as Pd, Pt, or Rh have been shown to promote H_2 activation and aid hydrogen spillover [8,26,27]. Sun et al. investigated the role of In_2O_3-supported Pt catalysts for CO_2 hydrogenation [28]. They found Pt/In_2O_3 highly selective towards methanol and used DFT calculations to investigate the reaction mechanism. Their results indicated electron transfer from In_2O_3 to the Pt_4 cluster, and this interfacial site promoted the dissociation of CO_2, suggesting the importance of SMSI effects and the more significant role of In_2O_3 in CO_2 hydrogenation.

When investigating Ga_2O_3 as a support it is important to note that there are a variety of Ga_2O_3 phases, including α-Ga_2O_3, β-Ga_2O_3, γ-Ga_2O_3, δ-Ga_2O_3, and ϵ-Ga_2O_3, which could impact catalytic behaviour [29–31]. Sharma et al. investigated diverse structural and electronic features of Ga_2O_3, highlighting the role of Ga^{3+} at the tetrahedral and octahedral sites and the behaviour regarding the various oxygen sites [29]. Amongst metal oxide supports, Ga_2O_3 possesses interesting structural and electronic properties [29,32] and has been explored as a support for metal nanoparticles for CO_2 hydrogenation to methanol [33–36].

The Pd_2Ga alloy has been studied for methanol synthesis from CO_2 hydrogenation [37–41]. Fujitani et al. investigated various 10 wt% Pd catalysts supported on different metal oxides and reported methanol yield at 5 MPa and 523 K in the order of $Ga_2O_3 > ZnO > Al_2O_3 > TiO_2 \approx Cr_2O_3 > SiO_2 \approx ZrO_2$ [37]. Pd/Ga_2O_3 gave rise to 10.1 % methanol yield. In contrast, Cu/ZnO resulted in only 4.2 % methanol yield [37]. The authors attributed this to the optimal concentration of Pd^{n+} stabilised by Ga_xO_y, and the mechanism occurring on Ga_2O_3 is less favourable to the RWGS reaction, unlike Pd supported on TiO_2 or Al_2O_3 which often results in high CO selectivity. Manrique et al. also attributed enhanced methanol selectivity for Pd/Ga_2O_3 catalysts but attributed this to the formation of Pd-Ga bimetallic nanoparticles, which reduced RWGS activity compared to monometallic Pd nanoparticles supported on SiO_2 [38]. The nature of the active sites in Pd-Ga catalysts were studied further by varying the molar ratio of Pd/Ga in $PdGa/SiO_2$ catalysts [39]. Here it was shown that when the Pd/Ga ratio was equimolar, the highest rate of methanol production was achieved. The Pd_2Ga alloy was observed with small amounts of excess Ga_2O_3 on the surface. However, when the Pd/Ga ratio was increased further, a layer of Ga_2O_3 covered the Pd_2Ga active sites which was detrimental to catalytic activity. Therefore, excess Ga_2O_3 showed negative consequences to this system. EXAFS studies were utilised to show the thin layer of Ga_2O_3 over the Pd_2Ga nanoparticles on the SiO_2 support [40]. However, in contrast to this, Liu et al. found depositing a thin layer of Ga_2O_3 over Pd/Ga_2O_3, via atomic layer deposition (ALD), aided in the formation of a Ga-rich alloy post-reduction which enhanced TOF values almost 10-fold [41].

We compare commercial In_2O_3 and Ga_2O_3 supports and their high surface area versions (prepared by ammonium carbonate precipitation) for their ability to catalyse the conversion of CO_2 and H_2 into methanol. We then go on to investigate the influence of adding Pd and Pd+Zn, their reactive interactions with the support, the influence on their efficacy for methanol synthesis and the overall mechanism of the reaction.

2. Experimental

2.1. Catalyst synthesis

Two forms of each oxide were used in this work, both commercially available samples and in-house synthesised oxides. Commercial In_2O_3 (denoted as In_2O_3-1, 99.99 %, Sigma Aldrich) and Ga_2O_3 (Ga_2O_3-1,

99.9+ %, Sigma Aldrich) were used, and synthesised In_2O_3 (In_2O_3-2) and Ga_2O_3 (Ga_2O_3-2) were made to compare with these.

Ga_2O_3 and In_2O_3 were synthesised via a precipitation method adapted from a ZnO preparation method reported previously [42,43]. For Ga_2O_3, stock solutions of $Ga(NO_3)_3.xH_2O$ (0.5 M, 99.999 %, Sigma Aldrich), and $(NH_4)_2CO_3$ (1 M) were prepared and stirred for 1 h. A 250 ml glass beaker was charged with 50 ml of the nitrate precursor solution, followed by rapid addition of 50 ml $(NH_4)_2CO_3$ solution under vigorous stirring. The mixture was heated in an oil bath to 60 °C and aged for 3 h. The precipitate was filtered, washed with 2 L deionised water, and then dried in a conventional oven at 110 °C for 16 h. The metal carbonate was calcined in air at 500 °C for 3 h. The above method was also applied for the preparation of In_2O_3 using an $In(NO_3)_3.xH_2O$ precursor (99.99 %, Sigma Aldrich).

Metal loaded catalysts were prepared using a solvent-free deposition technique called chemical vapour impregnation (CVI) and the Pd loading was aimed to be 5 wt%. For the preparation of the Pd catalysts $Pd(acac)_2$ (99 %, Sigma Aldrich) and the oxide were physically mixed in a glass vial for 1 min. The mixture was transferred to a Schlenk flask and sealed. The tube was connected to a vacuum line and evacuated (~10^{-3} mbar). The tube was lowered into an oil bath preheated to 80 °C and the temperature was increased to 133 °C and maintained for 1 h. The material was then recovered and calcined in static air (500 °C, 5 °C/min, 16 h). The calcined sample was then reduced in 5 % H_2/Ar (400 °C, 5 °C/min, 1 h). For PdZn catalysts the same procedure was used, mixing in Zn $(acac)_2$ (99 %, Sigma Aldrich) with the $Pd(acac)_2$ and the oxide, with a Pd:Zn molar ratio aimed to be 0.2.

2.2. Characterisation

Microwave digestion of catalysts using aqua regia was used, followed by ICP-MS to quantify total metal loading. The metal catalysts were digested (10 mg of catalyst, 1 ml of aqua regia, microwave-assisted acid digestion), filtered and diluted to a metal concentration of 10 ppm. Metal concentrations were determined using an Agilent 7900 ICP-MS with an I-AS autosampler.

Surface areas were analysed using a Quantachrome Nova 2200e instrument and calculated by the BET method. 5-point analysis was performed at – 196 °C. Prior to BET analysis samples were degassed under vacuum (150 °C, 3 h).

Powder X-ray diffraction (XRD) patterns were measured on a PANalytical X'pert Pro powder diffractometer operating at 40 kV, 40 mA using Cu Kα radiation ($\lambda = 1.54 \times 10^{-10}$ m) with a Ge (111) single crystal monochromator.

In situ XRD measurements were recorded on a (θ-θ) PANalytical X'pert Pro powder diffractometer. A Cu Kα radiation source (40 kV, 40 mA) was fitted with a position sensitive detector and an Anton Parr XRK reaction cell. The gas flow was controlled through a Bronkhorst mass flow controller, set to 30 ml/min (5 % H_2/Ar). The temperature was ramped from 50 °C - 500 °C, at 40 °C/min, with measurements conducted at 50 °C intervals.

XPS were recorded on a Kratos Axis Ultra-DLD photoelectron spectrometer, utilising monochromatic Al Kα radiation operating at 150 W power (10 mA x 15 kV). All spectra were recorded using a pass energy of 40 eV and step size of 0.1 eV for high resolution spectra, whilst survey spectra were recorded using a pass energy of 160 eV. All samples were mounted for analysis by pressing onto silicone free double-sided adhesive tape attached to a glass slide to allow isolation from the spectrometer. All data were acquired using a magnetically confined electron-only charge compensation system, and the charge was corrected to the C 1 s signal at 284.8 eV. Transmission corrected XPS data were analysed using Casa XPS software (v2.3.26 PR1.0 N) after subtraction of Shirley background and using modified Wagner sensitivity factors as supplied by the instrument manufacturer [44].

Scanning Electron Microscopy was performed on a Tescan MAIA3 Field Emission Gun (FEG - SEM) operating at 15 kV. Sample were

mounted on adhesive carbon Leit discs and analysed uncoated.

Transmission electron microscopy (TEM) was performed on a JEOL JEM-2100 operating at 200 kV. Energy dispersive X-ray analysis (EDX) was performed using an Oxford Instruments X-MaxN 80 detector and the data was analysed using Aztec software. Samples were prepared by dry dispersion over 300 mesh copper grids coated with holey carbon film.

Scanning transmission electron microscopy (STEM) was performed using a JEOL ARM200F microscope at the electron Physical Sciences Imaging Centre (ePSIC) at Diamond Light Source. An acceleration voltage of 200 kV, a convergence semi-angle of 23 mrad and a high-angle annular dark field (HAADF) inner angle of 80 mrad were used for data collection. Energy dispersive X-ray (EDX) spectrum imaging was performed using a JEOL Centurio dual detector. Samples were subsequently also imaged using a probe-corrected 200 kV Thermo-Scientific Spectra 200 Scanning Transmission Electron Microscope, at an accelerating voltage of 200 kV and with a convergence semi-angle of 30 mrad. The HAADF detector had an inner collection angle of approximately 56 mrad (outer angle of approximately 200 mrad). EDX spectrum images were acquired on a Super-X detector using all 4 detectors.

Catalyst Testing. Catalytic testing for CO_2 hydrogenation was carried out using a 16-bed high throughput catalytic reactor, designed, and manufactured by Integrated Lab Solutions GmbH (ILS). Integrated Workflow manager, based on LabView software, was used to operate the reactor with automation controlled by Siemens Win CC software. All beds in the reactor were operated under the same reaction conditions, with a fixed bed, continuous flow design. The gas feed was fed through a capillary distribution system and Equilibar back pressure regulators were used to control the pressure in each bed. To manage the reaction temperature, a thermocouple was positioned inside each of the four heating blocks, containing four beds each. Stainless steel reactor tubes with an internal diameter of 4.00 mm were used. Pelleted catalysts (0.5 g, 425–600 μm), mixed with F80 silicon carbide (mean particle size 190 μm) were centred in the isothermal zone and supported on a bed of F24 silicon carbide (particle size 750 μm), to limit mass transfer. The catalysts were reduced *in situ* in a flow of 5 % H_2/N_2 gas (400 °C, 1 h, 5° C/min) prior to testing, and subsequently cooled to 125 °C under N_2. The reactant gas composition used was 20 % CO_2, 60 % H_2, 5 % Ar, 15 % N_2, with a flow rate of 30 ml min^{-1} at atmospheric pressure. The system was pressurised to 20 bar and left to stabilise for 4 hrs before beginning the reaction. The reaction was conducted at 230 °C, 250 °C and 270 °C. To limit product build-up in the downstream lines, a purge feed of nitrogen (30 ml min^{-1}) was used and the downstream oven was set to 120 °C. The products were analysed *via* online gas chromatography (Agilent 7890B system with two flame ionisation detectors (FID) and a thermal conductivity detector TCD). Argon was used as an internal standard. Four injections per bed were taken at each temperature, and the Vici stream selection valve was switched between the beds to allow sampling of the products. From the moles of CO_2 in the calibration at 125 °C compared to the moles of CO_2 at each temperature for each bed, CO_2 conversion was calculated. Methanol, methane and CO were the main products observed. The carbon balance was calculated using the sum of carbon containing products and reactants in the feed divided by the sum of carbon containing reactants in the calibration runs. Catalyst testing errors were calculated by running 12 commercial $Cu/ZnO/Al_2O_3$ (CZA) standards using conditions stated.

3. Results and discussion

3.1. In_2O_3 and Ga_2O_3 structure

XRD was performed to determine the phase and crystallinity of the commercial In_2O_3, and the synthesised In_2O_3, labelled as In_2O_3-1, In_2O_3-2, respectively (Figure S1 and Table 1). The XRD reflections show a highly crystalline material for In_2O_3-1 with a sharp, intense reflection at 30.6°. The diffraction peaks for both are indexed to the diffraction pattern of cubic In_2O_3 (JCPDS 00–006–0416), but the synthesised In_2O_3

Table 1
Properties of the oxide samples.

Sample	Type	Phase from XRD	Particle size/nm	Surface[d] area/m^{2}g^{-1}
In₂O₃-1	Sigma Aldrich 99.99 %	Cubic	56[a]	25
In₂O₃-2	Synthesised	Cubic	12[a]	94
Ga₂O₃-1	Sigma Aldrich 99.9+ %	Monoclinic / β-Ga₂O₃	134[b]	8
Ga₂O₃-2	Synthesised	Rhombohedral / α-Ga₂O₃	65[c]	47

[a] determined from the (222) plane in XRD using Scherrer equation.
[b] using the (111) plane.
[c] using the (110) plane.
[d] BET method.

shows much broader peaks, suggesting a small crystallite size of In_2O_3. Average crystallite sizes were calculated using the Scherrer equation, see Table 1. In_2O_3-1 has a crystallite size of 56 nm, whereas the synthesised In_2O_3-2 is much smaller at 12 nm. The specific surface area also reflects the crystallite size, resulting in an almost 4-fold increase in surface area for In_2O_3-2 of 94 m^2/g (compared to 25 m^2/g for In_2O_3-1).

For Ga_2O_3, again two forms of the material were used, one commercial and one synthesised as described in the experimental section, labelled as Ga_2O_3-1, Ga_2O_3-2, respectively. XRD was used to compare the commercial and synthesised gallium oxide regarding phase, structure, and crystallite size Figure S2, Table 1. Amongst the five different polymorphs of Ga_2O_3, α-Ga_2O_3 (rhombohedral) and β-Ga_2O_3 (monoclinic) are the most common compared to γ-Ga_2O_3 (defective spinel), δ-Ga_2O_3 (cubic), and ε-Ga_2O_3 (orthorhombic) [29]. Ga_2O_3-1 shows a monoclinic crystal structure compared to a rhombohedral crystal structure for synthesised Ga_2O_3-2, Figure S2. Monoclinic (β-Ga_2O_3) is the most stable polymorph and above certain conditions (> 600 °C), the other polymorphs can convert into β-Ga2O3 [45]. Ga2O3–2 showed broader Bragg peaks than Ga_2O_3-1, again indicative of smaller nanoparticles [46].

The materials were also characterised by FEG-SEM to explore surface morphology. The SEM micrograph in Figure S3 for In_2O_3-1 shows that platelets are formed, with evidence of some smaller clusters. Figure S4 shows the morphology of the prepared In_2O_3-2 with increased surface area, and this shows finer aggregate particles. Commercial Ga_2O_3-1 comprises a porous rod-like structure, Figure S5a and b, with a surface area of 8 m^2/g (Table 1). In comparison, synthesised Ga_2O_3-2 showed much smaller rod-like structures (Figure S6a, b). Through precipitation using ammonium carbonate, the surface area increased 6-fold to 47 m^2/g, Table 1.

As reported by others [14,15], indium oxide shows good selectivity and activity to methanol during CO_2 hydrogenation, whereas gallium oxide seems to be inactive [6]. Similar behaviour was found here. The relevant data for the reactivity of the materials used here is shown in the next section which considers the effects of Pd addition.

3.2. CO_2 hydrogenation on Pd loaded catalysts and the effect of Zn addition

Table S1 summarises the elemental analysis and the surface areas for the catalysts used. Pd loadings are synthesised to be 5 wt%, and when Zn is incorporated, the Zn/Pd molar ratio used is aimed to be 5, equivalent to ~15 wt% Zn. As can be seen the Pd levels are fairly close to these values, though the Zn loading is generally somewhat lower, especially for the commercial PdZn/Ga_2O_3-1, at 10.7 wt%. Regarding surface area, as shown in Table S1, commercial In_2O_3 has a surface area of 25 m^2/g, and when Pd is deposited onto In_2O_3-1, the surface area remains similar at 22 m^2/g, and incorporating Zn then reduced the surface area to 17 m^2/g for PdZn/In_2O_3-1. The surface area of the synthesised In_2O_3 is

much higher than that of the commercial In$_2$O$_3$, with a surface area of 94 m^2/g. However, with the addition of Pd and PdZn, the catalyst surface area of In$_2$O$_3$-2 decreased significantly. Therefore, the high surface area is not sustained during catalyst preparation. The Ga$_2$O$_3$ samples also lose their area, but not to such a great extent: the synthesised versions lose ~ 40 % of their area during CVI and subsequent treatment (Table S1).

All the catalysts were tested for CO$_2$ hydrogenation at three temperatures after pre-reduction *in situ* in the reactor, and the results are displayed in Fig. 1, Table S2 and Figs. S7–9. Most oxides we have examined under these conditions have immeasurable conversion, but this is not the case for In$_2$O$_3$, as reported by several authors previously [14,15]. In the current work the conversion for both commercial and synthesised oxides was significant, with the latter, shown in Fig. 1a, having a little higher conversion. Commercial In$_2$O$_3$ has higher initial selectivity, but this declines rapidly with increasing temperature, while the decline for synthesised In$_2$O$_3$-2 is much less severe. Ga$_2$O$_3$ has no activity under these conditions. We consider that the main reason for the difference between the two oxides is reducibility, which in turn, for these trivalent oxides, reflects their enthalpy of formation. The enthalpy of reduction for the two oxides is ~80 kJ/mol for In$_2$O$_3$ and 235 kJ/mol for Ga$_2$O$_3$.

Generally, when Pd is added to oxide catalysts by CVI small nanoparticles are formed (see electron microscopy below) and then there is a significant increase in conversion. This is particularly so for ZnO [37,43, 47–50] and Ga$_2$O$_3$ [37–41]. This is also true here for Pd/In$_2$O$_3$ in Fig. 1, but to a much lesser extent than with other oxides, since the In$_2$O$_3$ itself is active. The conversion at 270 °C increases from 4 % to 6 %, while the selectivity increases from 57 % to 75 %, and at 230 °C it is very high at ~88 % for both Pd/In2O3 catalysts. The conversion for Ga$_2$O$_3$ is much higher than for the In catalysts, being approximately doubled at each temperature, whereas the selectivity is lower, mainly due to the higher conversion. Methanol production rates for these materials are shown in supplementary Table S2 and Figs. S7–9 and in the associated text. The highest productivities for the In-supported catalysts are achieved with the Pd-loaded synthesised indium oxide catalyst, Pd/In$_2$O$_3$-2, whereas the opposite is the case for the Ga catalysts – the commercial sample has the higher overall productivity. In Fig. 1 we have also shown data for Pd/ZnO, also made by CVI of Pd, which produces a β-PdZn 1:1 alloy [51–54] after reduction. Here it can be seen that the activity is a little higher than the Ga$_2$O$_3$ materials under the same conditions, and the selectivity is higher.

When Zn and Pd are co-deposited on In$_2$O$_3$ catalysts, Fig. 1b and S7-

S9 and Tables S1 and S2, the effects are slightly negative, both on activity and selectivity. On the other hand, when Zn is added to the Pd/Ga$_2$O$_3$ samples there is a positive effect, especially on conversion for sample 2 (conversion at 230 °C increases from 4.5 % to 7 %) and more for selectivity on sample 1 (increased from 50 % to 67 %). Hence in both latter cases overall methanol productivity is enhanced by the addition of Zn (Table S2).

Note that the best catalysts (the Zn based ones) are operating close to equilibrium at the highest temperature (equilibrium conversion ~ 21 %, methanol selectivity and yield ~ 19 % and ~4 % [55,56]), but not at 230 °C (see Table 2).

3.3. Catalyst structure and alloy formation

To understand these reactivity patterns characterisation of these catalysts was needed, and the main techniques used were XRD, XPS and electron microscopy, as follows.

3.3.1. Pd/In$_2$O$_3$ and PdZn/In$_2$O$_3$

XRD patterns are shown in Figs. 2 and S10 for reduced Pd and PdZn-supported catalysts on In2O3–1 and In2O3-2. All of the In$_2$O$_3$ patterns correspond to the cubic phase (JPCS 00–006–0416). PdZn/In$_2$O$_3$-1 and PdZn/In$_2$O$_3$-2 also show the characteristic reflections of ZnO at 31.8°, 34.4° and 36.3°.

Fig. 2 shows the reference pattern of indium oxide together with those after addition of Pd and Zn. For the Pd/In$_2$O$_3$ samples, there is clear differentiation of ~ 0.2° between reflections at 39.9 and 40.1°, which could correspond to Bragg peaks from several contributions, namely either Pd, PdIn or Pd$_2$In$_3$. PdIn(110) may be in this precise region [51,52]. Additionally, the slight splitting of the reflection, which could correspond to overlapping (110) and (012) Pd$_2$In$_3$ reflections at 39.9° and 40.1° could have a contribution from Pd(111), which is also at 40.1°. However, we eliminate the possibility of significant amounts of

Table 2
Equilibrium methanol conversion, selectivity and yields, taken from Zhong et al. [55] and Shen et al. [56], compared with the best experimental yields.

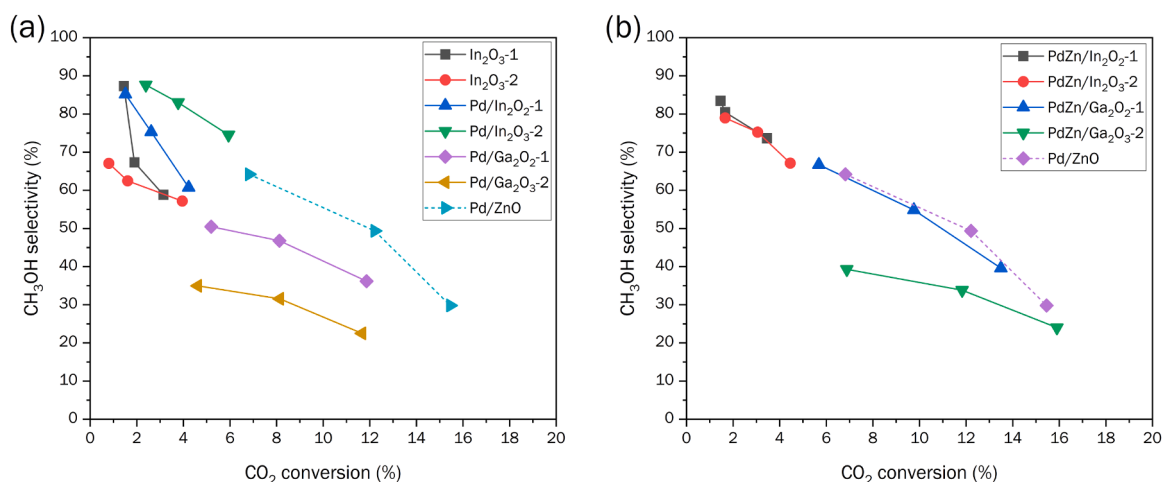| Temperature/ °C	Selectivity/ %	Conversion/ %	Yield/ %	Best experimental yield/%
230	54	18	10	4.5
250	35	19.5	7	6.0
270	19	21	4	4.5

Fig. 1. a) CO$_2$ conversion vs CH$_3$OH selectivity for the catalysts studied here. The three data points for each sample correspond to increasing reaction temperatures, from left to right, of 230, 250, and 270 °C, also corresponding with increasing conversion. Data for Pd/ZnO are added for comparison. All the metal loaded catalysts are made by CVI with a nominal 5 % weight loading. b) CO$_2$ conversion vs CH$_3$OH selectivity for the catalysts in a) but now with Zn added (Pd:Zn molar ratio 0.2) and compared with 5 wt% Pd/ZnO.

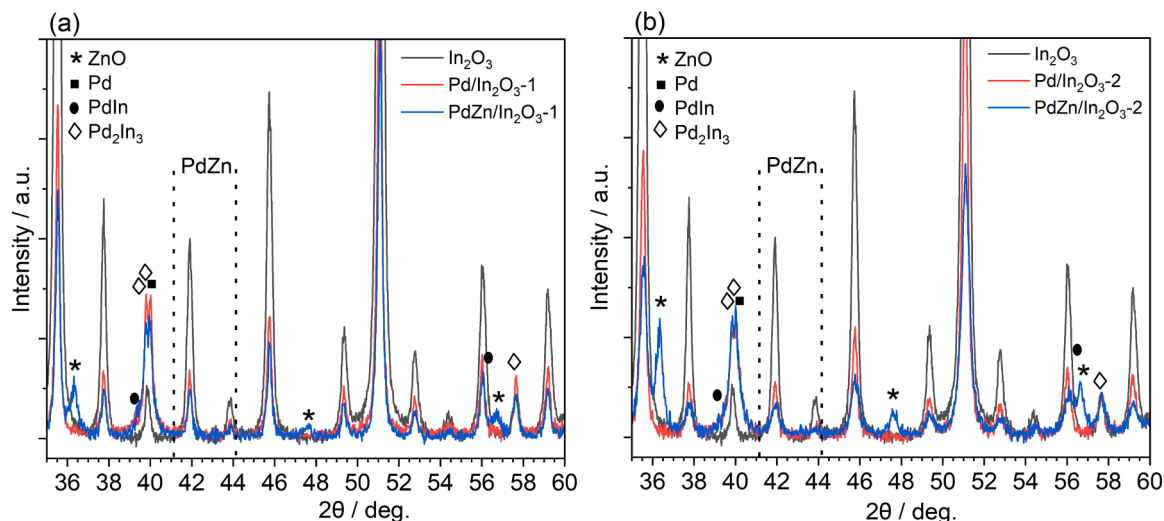**Fig. 2.** XRD reflections for In$_2$O$_3$-1, Pd/In$_2$O$_3$-1, PdZn/In$_2$O$_3$-1, Pd/In$_2$O$_3$-2, and PdZn/In$_2$O$_3$-1 catalysts (5 wt% Pd, Zn/Pd = 5), after reduction (400 °C, 1 h, 5 % H$_2$/Ar).

Pd metal, since the (200) Bragg peak at 48.5° is missing. So, we consider the peaks at 39.9 and 40.1° to be from the Pd$_2$In$_3$ alloy. Additionally, at 57.7° a reflection corresponding to Pd$_2$In$_3$ should also be observed but this overlaps with an In$_2$O$_3$ reflection. However, the other In$_2$O$_3$ reflections have been much reduced in the Pd pattern (simply due to changes in machine intensity), whereas the 57.7° reflection remains at the same intensity because there are contributions to it from both the In$_2$O$_3$ and the Pd$_2$In$_3$ alloy. It is notable also that for Pd/ZnO catalysts
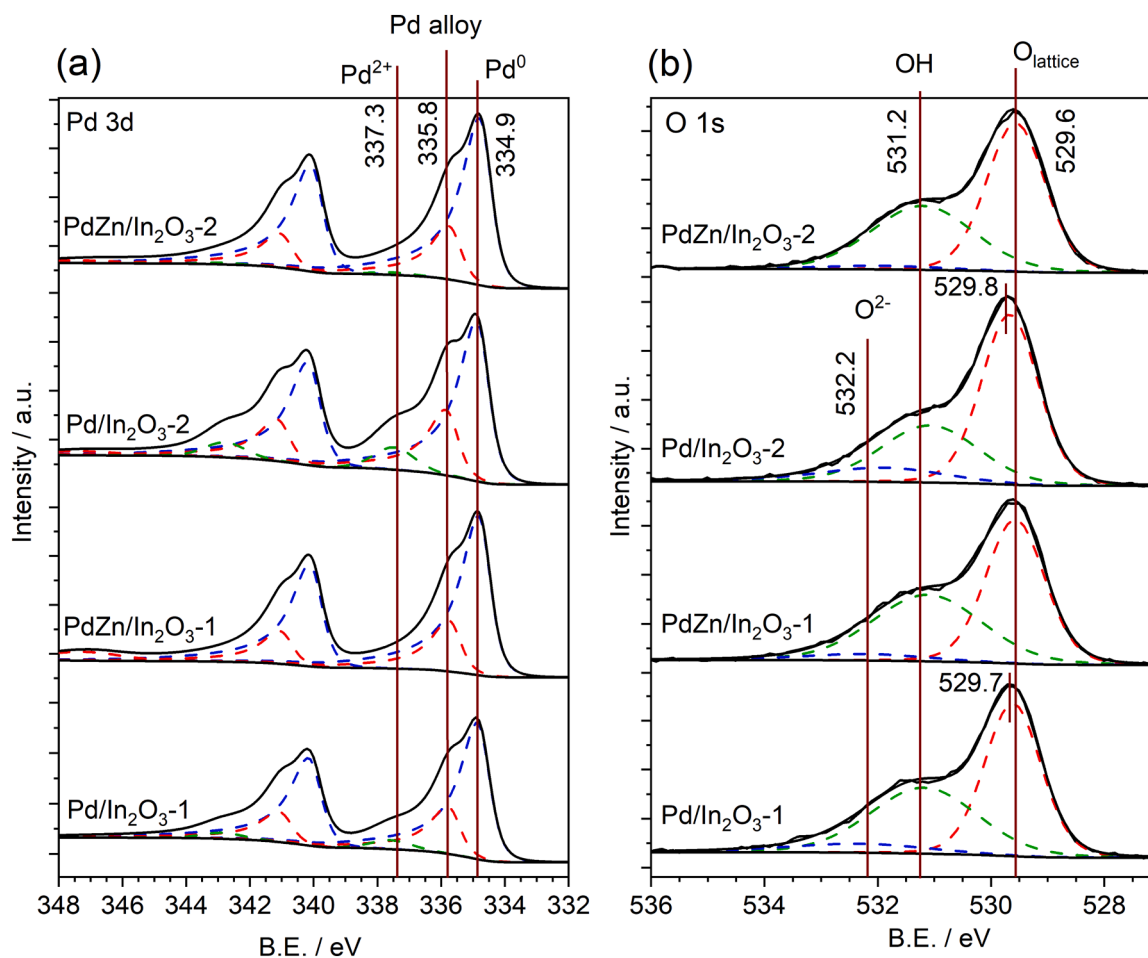
Fig. 3. XPS fittings for (a) Pd 3d with fittings for Pd^0 (blue), Pd alloy (red), Pd^{2+} (green), and (b) O 1 s with fittings for O$_{lattice}$ (red), OH (green), O^{2-} (blue), for Pd/In$_2$O$_3$-1, PdZn/In$_2$O$_3$-1, Pd/In$_2$O$_3$-2, PdZn/In$_2$O$_3$-2. Prior to XPS analysis, materials were reduced ex situ (400 °C, 1 h, 5 % H2/Ar), but were air-exposed before the measurements during transfer.

the β-PdZn alloy (the characteristic 1:1 β-PdZn alloy reflections are at 41.4 and 44.1°) is readily formed upon reduction, but when Zn is added here (Fig. 2) it does not form. The Pd_2In_3 alloy is preferred.

García-Trenco et al. attributed enhanced methanol selectivity (> 80 %) to the bimetallic PdIn alloy [8]. Snider et al. also found that a bimetallic PdIn compound in conjunction with an indium oxide phase maximised methanol synthesis [53]. Similar catalytic performances to PdIn were also found in a non-precious metal catalysts containing a binary system of InNi [53]. However, Frei et al. synthesised a palladium promoted In_2O_3 catalyst via coprecipitation and found it to be more stable with higher methanol selectivity compared to the same catalyst prepared by dry impregnation [54]. They proposed that PdIn was not formed, but that palladium was atomically dispersed in the oxide matrix increasing stability. The number of oxygen vacancies did not increase, but favourable electronic properties enabled improved H_2 dissociation, and the small size of the palladium cluster suppressed the RWGS and promoted methanol [54].

XPS was employed to further investigate potential PdIn alloying, as seen in Fig. 3. The binding energies at 334.9 eV indicate Pd metal, suggesting the presence of Pd on the surface of In_2O_3, Fig. 3a [8,9,53,54, 59]. However, a clear shoulder is observed in all of the samples at 335.8 eV, corresponding to a Pd alloy, in accordance with previous reports in literature [8,55]. Some contributions by PdO can be observed in Pd/In_2O_3-1 and Pd/In_2O_3-2 at 337.3 eV, most likely from exposure to air before conducting the XPS experiments. It is notable that this is not so obvious for the PdZn materials, implying more resistance to surface oxidation.

Pd/In_2O_3-2 displayed the highest catalytic performance in this series, and superior activity has often been associated with increased oxygen vacancies [21]. Fig. 3b shows O 1 s XPS data for Pd/In_2O_3-1, PdZn/In_2O_3-1, Pd/In_2O_3-2, PdZn/In_2O_3-2. The 529.8 eV peak originates from the oxygen in In-O-In ($O_{lattice}$) [17], and the overlapping peak at 531.2 eV can be assigned to hydroxyl groups (OH) [37]. Table 3 displays the ratio of the $O_{lattice}$ and the O associated with hydroxyl groups in the O 1 s XPS spectra. Pd/In_2O_3-2 displays fewer OH contributions, which are commonly associated with OH adsorbing on oxygen vacancies, but shows the highest catalytic performance in this series, in tentative agreement with the proposals of Dang et al. [21]. Other than this there was very little difference observed in XPS between the catalysts produced on the two different supports.

Previous studies have often utilised O 1 s XPS data to ascribe oxygen species from the lattice, vacancy sites, defects, or surface hydroxyl species. Idriss nicely described common misinterpretations in O1s spectra when discussing oxygen vacancies in metal oxides [19]. It was proposed that hydroxyl groups are detected in XPS at ambient conditions. Dissociated water on the surface of the oxide may occur from adsorption at oxygen vacancies. Based upon Idriss's work, Frankcombe and Liu employed computational modelling to ascribe appropriate fittings in O 1 s spectra from ZnO [18]. Lattice oxygen dominated at 530 eV, in this case, and an increase in binding energy was attributed to surface water strongly binding, through chemisorption or surface hydroxyl groups. This provided critical insight into oxygen vacancy interpretations of XPS data, contradicting many published articles.

Going forward, it seems more in-depth understanding and critically reviewing data is required for assigning oxygen vacancies. It must be noted that the work examined *ex situ* experiments; therefore, the

importance of *in situ* characterisation will aid in improving these limitations of surface -OH species. The peaks in the region of ~529.6 eV are related to the overlapping of the O^{2-} associated in ZnO (previously reported at 529.8 eV) and the O 1 s peak relating to the lattice O in In_2O_3 [20].

Further support for alloy formation from XPS is given in the supplementary text and Figure S11

To investigate morphological differences and particle sizes after the addition of Pd and Zn, Fig. 4 displays the micrographs and the corresponding histograms for particle diameter distributions for Pd/In_2O_3-1, PdZn/In_2O_3-1, Pd/In_2O_3-2, PdZn/In_2O_3-2 post-reduction catalysts (400 °C, 1 h, 5 % H_2/Ar). The catalysts contain roughly spherical particles with an average diameter of ca. 8–11 nm, an average for around 100 particles for each sample.

Interestingly, a rather thick shell-like overlayer, which might tentatively correspond to In_2O_3, surrounds some particles upon magnification (Fig. 5). Upon evaluation of the In_2O_3-1 and In_2O_3-2 support, only Pd/In_2O_3-1 and PdZn/In_2O_3-1 showed the presence of some voids perhaps corresponding to a smaller $O_{lattice}$/OH ratio seen in the XPS O 1 s spectra, and perhaps due to the loss of In/In_2O_3 from the bulk to form the alloy and the overlayer.

STEM imaging was utilised to investigate potential alloy formation further. Bright-field imaging, High angle annular dark filed (HAADF), and energy dispersive X-ray (EDX) mapping is shown in Fig. 6 for Pd/In_2O-1 after reduction. A shell around the nanoparticle can be observed in the BF imaging, similar to the previous TEM images. Nanoparticles containing palladium can be clearly identified, but it also seems that indium is incorporated. XPS data suggested Pd alloy formation; therefore, it is likely that a Pd-In intermetallic species has formed in the nanoparticle. However, some presence of oxygen also suggests an In_2O_3 overlayer, which can be clearly seen in BF imaging due to greater contrast compared to the HAADF image.

Additionally, Fig. 7 shows another BF image of Pd/In_2O_3-1 with lattice fringing. The d spacing in the nanoparticle is measured to be 0.3 nm, which could be the (011) plane of the Pd_2In_3 alloy. A shell is also observed around the nanoparticle, most likely to be In_2O_3. Furukawa et al. and Skala et al revealed a core-shell structure of PdIn/SiO_2. The structure comprised a PdIn core with an In_2O_3 composition shell [57, 58].

The catalytic reactivity between In_2O_3-1 and Pd/In_2O_3-1 doesn't differ greatly, which could be attributed to the shell of In_2O_3 covering the PdIn nanoparticle. There is some improvement in selectivity for Pd/In_2O_3-2, as methanol productivity is improved by a factor of 2 compared to In_2O_3-2 at 270 °C, suggesting that, although the oxide dominates reactivity there are some positive synergistic effects between the metal nanoparticle and In_2O_3 despite an observed shell, presumably due to some electronic interaction with the underlying metal. However, compared with the effects on performance of the Ga-based catalysts, these changes are relatively minor, and the catalysts are less active than the Ga versions.

3.3.2. Pd/Ga_2O_3 and Pd/ZnO/Ga_2O_3

The series of reduced Pd and PdZn catalysts supported on Ga_2O_3-1 and Ga_2O_3-2 were investigated by XRD, Fig. 8 (and supplementary Figures S12, S13). Pd/Ga_2O_3-1 maintains the monoclinic Ga_2O_3 phase, and the Pd_2Ga alloy is detected at 39.7°, 40.2°, and 41.3°. Previous studies have reported that a variety of alloys can be present simultaneously [6,59,60]. However, no other Pd-Ga intermetallic compositions could be assigned when investigating the sample by XRD. PdZn/Ga_2O_3-1 shows the formation of the PdZn alloy, which seems to be preferred over other intermetallic compounds, such as PdGa or PdZnGa [10].

With regards to Pd/Ga_2O_3-2 (Fig. 8b), detection of Pd_2Ga is more challenging due to the overlap of rhombohedral reflections from the support. The broad reflection around 40.3° might be due to the overlap of multiple Pd-Ga alloys [61,62] with the Ga_2O_3 reflection [41]. For PdZn/Ga_2O_3-2, there is an overlap between the PdZn reflections and the

Table 3
The $O_{lattice}$/OH ratio for Pd and PdZn supported on In_2O_3.

Catalyst	$O_{lattice}$/OH
Pd/In_2O_3-1	1.2
PdZn/In_2O_3-1	1.2
Pd/In_2O_3-2	1.7
PdZn/In_2O_3-2	1.3
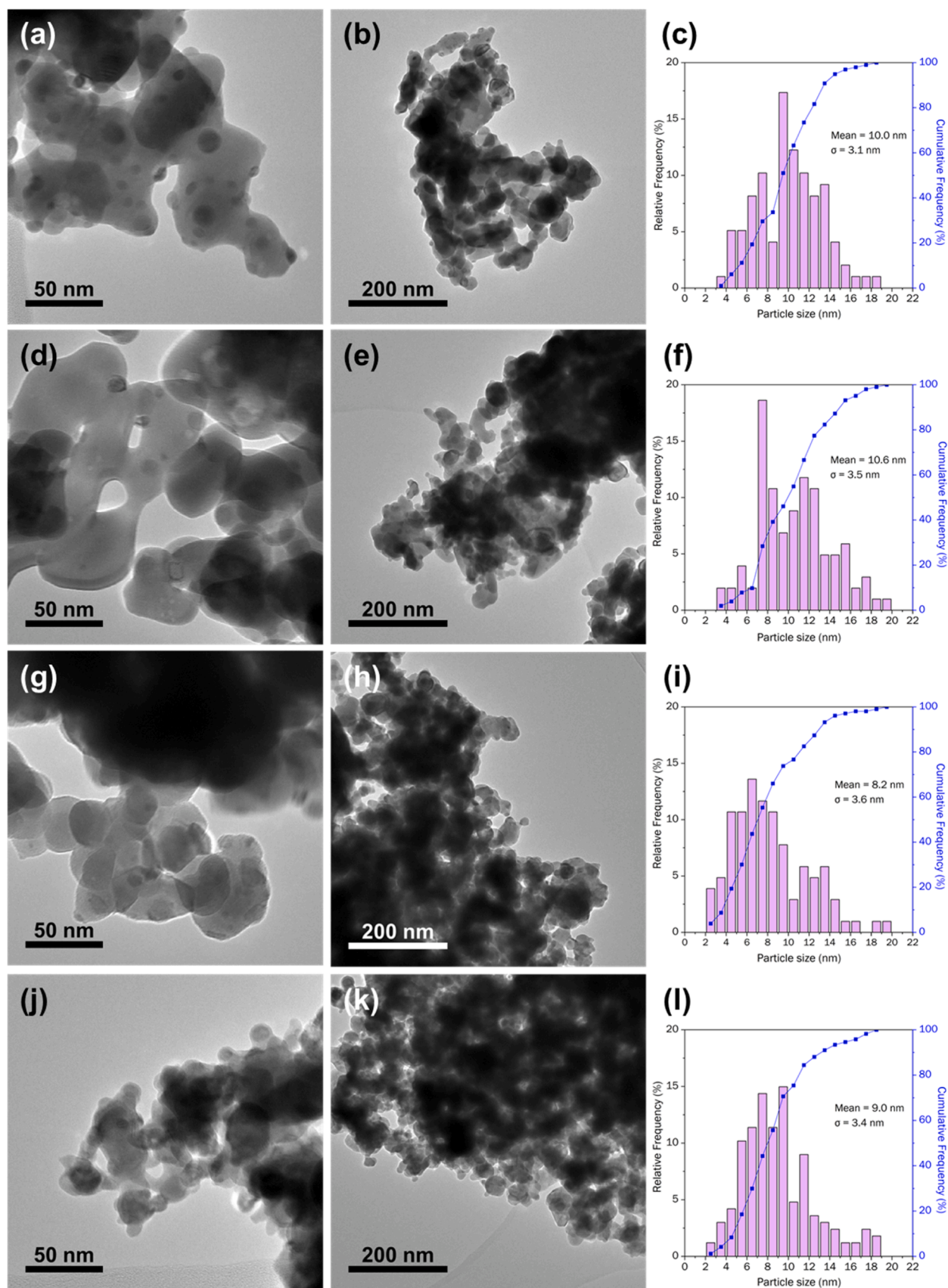
Fig. 4. Representative TEM images, and particle size distributions of Pd/In$_2$O$_3$-1 (a-c), PdZn/In$_2$O$_3$-1 (d-f), Pd/In$_2$O$_3$-2 (g-i), and PdZn/In$_2$O$_3$-2 (j-l). All catalysts were reduced at 400 °C for 1 h (5 °C min^{-1}) under 5 % H$_2$/Ar prior to analysis.
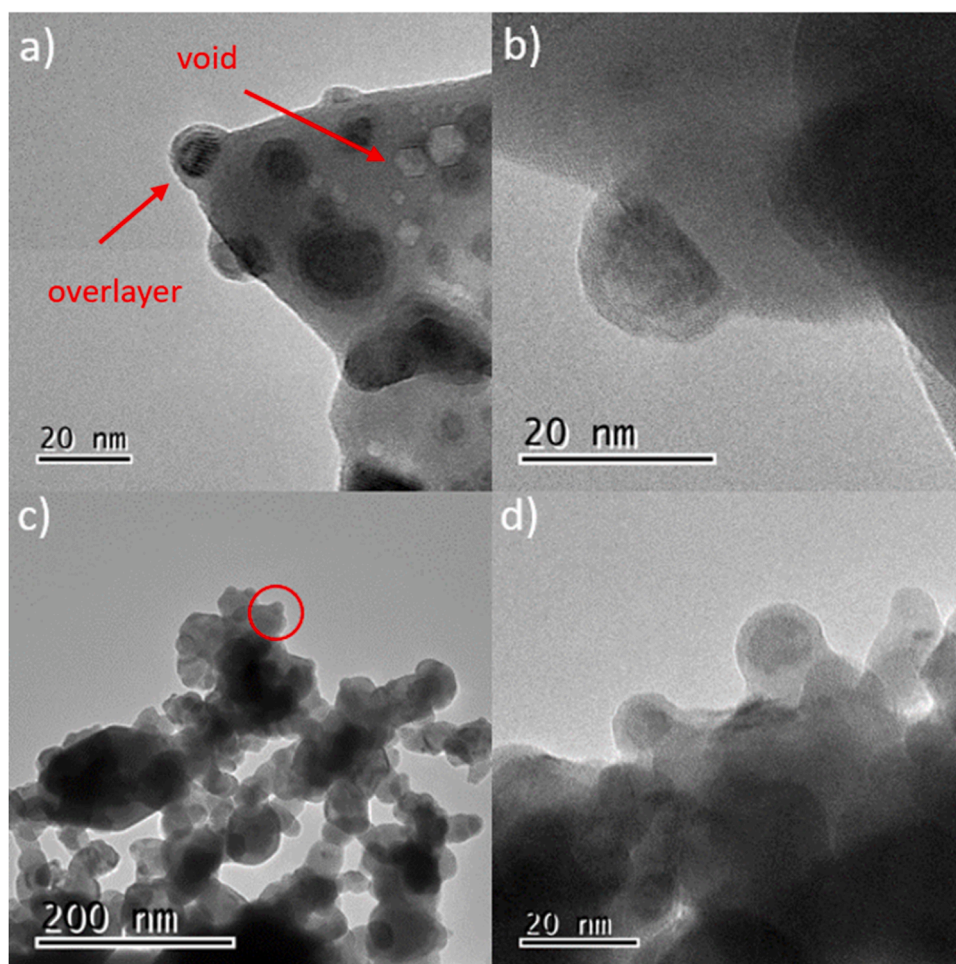
Fig. 5. Examples of particles with an overlayer, a) Pd/In$_2$O$_3$-1, b) PdZn/In$_2$O$_3$-1, c) Pd/In$_2$O$_3$-2 (red circle indicates overlayer), d) PdZn/In$_2$O$_3$-2.
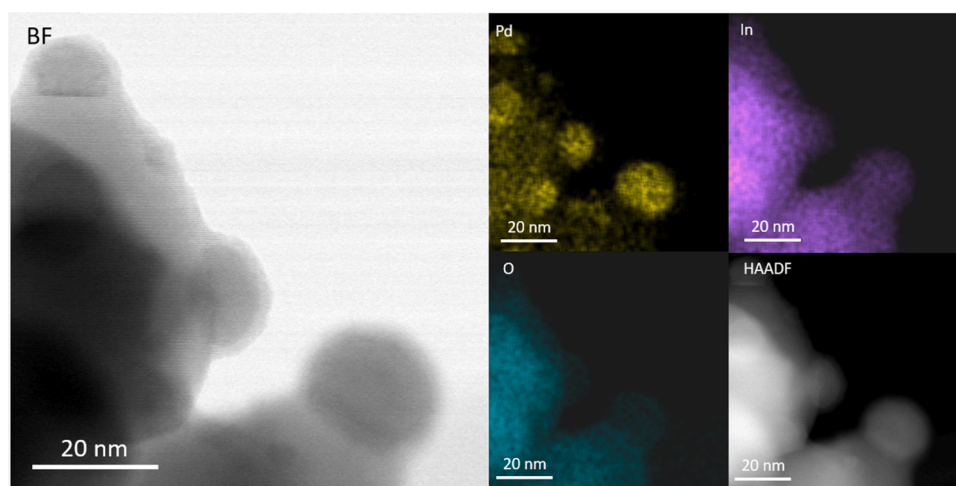
Fig. 6. Brightfield and EDX elemental mapping with corresponding HAADF image for Pd/In2O3-1 after reduction (400 °C, 1 h, 5 % H$_2$/Ar).

support. However, the broad peaks at 43.9° are due to the (110) plane of the PdZn alloy, in addition to the main reflection at 41.4°. ZnO reflections can be observed, suggesting excess ZnO is substantially available on the catalyst surface [6]. Interestingly, reflections at 30.4, 37.4, 43.5, and 57.4° are also detected for PdZn/Ga$_2$O$_3$-2 related to a ZnGa$_2$O$_4$ structure. Cored et al. found that changing the precipitating reagent to NaOH in a co-precipitation method for Cu/ZnO/Ga$_2$O$_3$, resulted in the

formation of Ga^{3+} doped ZnO, while the utilisation of NH$_4$HCO$_3$ led to the creation of ZnGa$_2$O$_4$ [61]. That study found that for CO$_2$ hydrogenation to methanol, surface enrichment of Ga^{3+} doped into the wurtzite ZnO lattice stabilised the Cu species and increased surface basic sites for CO$_2$ adsorption, leading to more favourable CO$_2$ conversion and methanol productivity compared to ZnGa$_2$O$_4$ [63]. However, Liu et al. showed that the ZnGa$_2$O$_4$ species was responsible for the hydrogenation
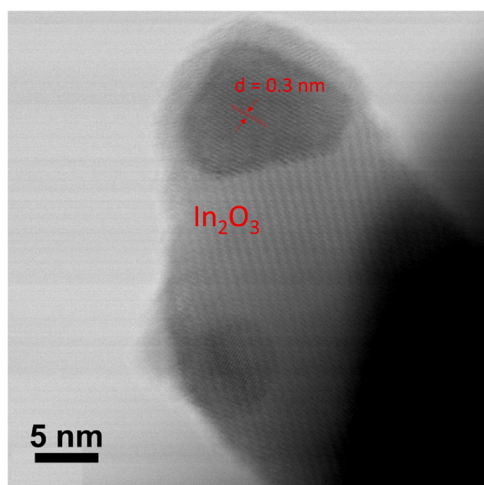
Fig. 7. BF image of Pd/In$_2$O$_3$-1 after reduction.
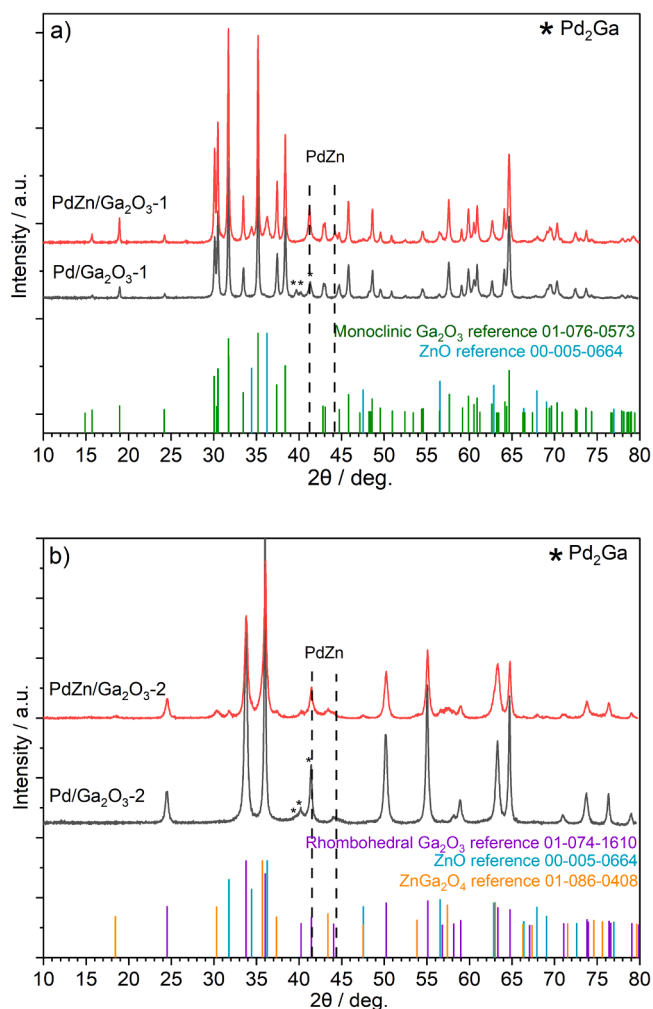

Fig. 8. X-ray diffraction patterns for a) Pd and PdZn supported on Ga$_2$O$_3$-1, b) Pd and PdZn supported on Ga$_2$O$_3$-2. Catalysts are reduced at 400 °C, 1 h, 5 % H$_2$/Ar.

of CO$_2$ to methanol due to surface oxygen vacancies providing CO$_2$ activation sites via formate and methoxide species [64]. This perhaps could correspond to a slight increase in CO$_2$ conversion that was observed in PdZn/Ga$_2$O$_3$-2. However, CO production dominates over

PdZn/Ga$_2$O$_3$-2 (75 % selectivity at 270 °C). Liu et al. also showed that coupling ZnGa$_2$O$_4$ with SAPO-34 suppressed the RWGS reaction and SAPO-34 was responsible for C-C coupling reactions to C$_2$-C$_4$ olefins [64]. Meng-Jung Li et al. also showed the beneficial impact of incorporating Ga^{3+} in Cu/ZnO due to the formation of ZnGa$_2$O$_4$ [65]. They suggested that the ZnGa$_2$O$_4$ structure created an electronic heterojunction with an excess ZnO phase to account for the reduction of Zn^{2+} to Zn^0 to form the active CuZn bimetallic nanoparticle [65].

To further investigate the extent of alloying for Pd and PdZn supported on synthesised Ga$_2$O$_3$, the samples were characterised by XPS as shown in Fig. 9, and Figs. S12 and 13, and are compared to the XPS spectra of Pd/Ga$_2$O$_3$-1 and PdZn/Ga$_2$O$_3$-1 after reduction. There is evidence of Pd alloying across all catalysts (340.6 – 341.1 eV); however, for Pd/Ga$_2$O$_3$-2 and PdZn/Ga$_2$O$_3$-2 Pd metal dominates at binding energies 334.8, 334.6 eV for Pd/Ga$_2$O$_3$-2, PdZn/Ga$_2$O$_3$-2, respectively. From XRD, as discussed previously, the assignment for PdGa or PdZn alloy formation is challenging due to overlapping reflections from rhombohedral Ga$_2$O$_3$; however, XPS was used to gain further insight into the nature of the metal nanoparticles and indicates formation of the Pd alloy. Interestingly, it seems that the alloy can form more readily on Ga$_2$O$_3$-1, compared to Ga$_2$O$_3$-2, as evident by the increased Pd metal peaks in Fig. 9c and d. The PdZn alloy peaks in the XPS due to the monoclinic Ga$_2$O$_3$ and the difference in alloy abundance could be associated with different Ga$_2$O$_3$ polymorphs facilitating different rates of hydrogen spillover by the metal nanoparticle under reducing conditions [66,67].

For Pd/Ga$_2$O$_3$-2 it is likely that the peaks at 335.7 and 340.9 eV correspond to Pd-Ga [10,41]. For PdZn/Ga$_2$O$_3$-2 the Pd alloy peak is similar to that observed in Pd/Ga$_2$O$_3$-2, however, from previous investigations, it is likely that the peaks at 335.6 and 335.3 eV correspond to PdZn [44] as seen previously with PdZn/Ga$_2$O$_3$-1. Studies have shown that the PdZn alloy is favoured over PdGa intermetallic species, despite the favourable heat of mixing for PdGa alloys but rather due to the lower stability of ZnO compared to Ga$_2$O$_3$, in a reducing environment, PdZn alloy formation is favourable [10]. This highlights the role of the metal oxide and its reducibility.

Average particle sizes and distributions for the Ga$_2$O$_3$-based catalysts were evaluated using TEM (Fig. 10). Micrographs were obtained on samples after reduction (5 % H$_2$/Ar, 400 °C, 1 h), and particle size histograms were obtained using image J software [68]; 100–200 particles were analysed for each catalyst to ensure representative particle size distributions. The morphology differences of the support can be observed; the higher surface area Ga$_2$O$_3$, synthesised by ammonium carbonate precipitation appears more porous. A broad particle size distribution and a high mean particle size of 12.7 nm is generated when Pd is supported on Ga$_2$O$_3$-1, whereas when incorporating Zn and forming the PdZn alloy, a lower mean particle size is observed for PdZn/Ga$_2$O$_3$-1 at 8.0 nm. As seen with PdZn/TiO$_2$, adding Zn above a Pd:Zn equimolar ratio increases methanol productivity, due to the bifunctional mechanism of the formed PdZn alloy and contact with the ZnO phase [4–6], it is therefore likely that the increase in methanol selectivity for the PdZn/Ga$_2$O$_3$-1 catalyst is due to the formation of the PdZn alloy in contact with ZnO, rather than a particle size influence.

However, when Pd and PdZn is supported on Ga$_2$O$_3$-2, mean particle sizes are smaller than that of Pd/Ga$_2$O$_3$-1 and little difference in particle size is observed between Pd/Ga$_2$O$_3$-2 and PdZn/Ga$_2$O$_3$-2, at 5.5 and 5.7 nm, respectively. The particle size distribution is relatively narrow for Pd and PdZn supported on synthesised Ga$_2$O$_3$-2. However, for commercial Ga$_2$O$_3$, it is evident that there is a wider range of particle sizes. An increase in CO$_2$ conversion is seen from 12 % to 16 % at 270 °C for Pd/Ga$_2$O$_3$-2 to PdZn/Ga$_2$O$_3$-2, but the insignificant change in particle size between the two catalysts suggests that it's the influence of the PdZn alloy, ZnO and possibly the formation of the ZnGa$_2$O$_4$ phase that is influencing CO$_2$ activation.

Scanning transmission electron microscopy (STEM) was used to verify alloying in Pd/Ga$_2$O$_3$ and PdZn/Ga$_2$O$_3$. HAADF-STEM images and
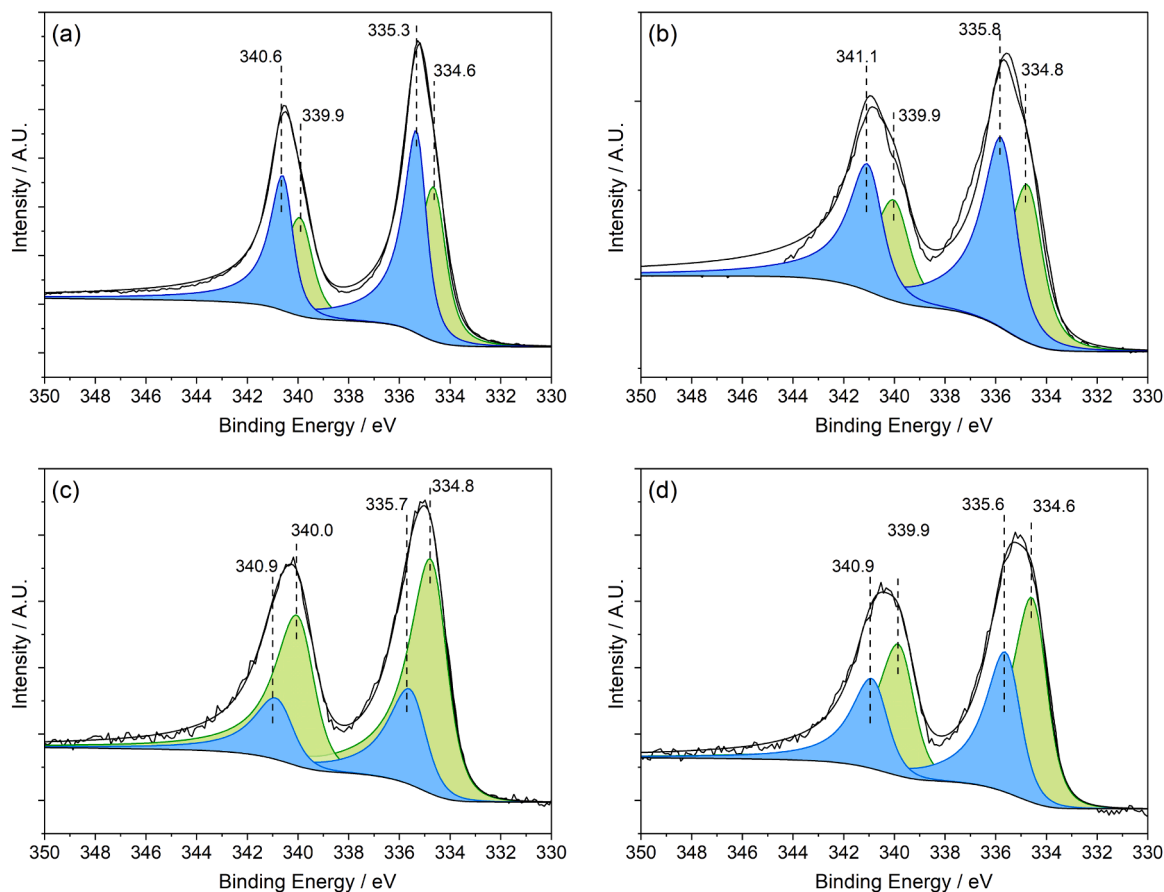
Fig. 9. Pd 3d XPS for (a) Pd/Ga$_2$O$_3$-1, (b) PdZn/Ga$_2$O$_3$-1, (c) Pd/Ga$_2$O$_3$-2, and (d) PdZn/Ga$_2$O$_3$-2 after reduction (400 °C, 1 h, 5 % H$_2$/Ar) Pd metal and alloyed Pd in the peak fitting are represented in green (~334.6 eV), blue (~335.7 eV), respectively.

elemental maps, using energy dispersive X-ray (EDX) spectroscopy of Pd/Ga$_2$O$_3$ and PdZn/Ga$_2$O$_3$ were acquired, where each sample had been reduced at 400 °C for 1 h in 5 % H$_2$/Ar (Fig. 11).

The upper panel of Fig. 11 clearly shows alloying between Pd and Ga in the Pd/Ga$_2$O$_3$-1 sample, and Ga is detected in the EDX spectrum obtained solely from the highlighted metallic nanoparticle. Regarding the PdZn/Ga$_2$O$_3$ sample (Fig. 11 lower panels), the STEM-EDX data supports the preferential formation of the PdZn alloy without the presence of Ga in the metal particles. The extracted elemental maps show a clear correlation between Pd and Zn, and the corresponding spectrum shows a minor level of Ga present, which could arise due to the proximity of the support.

HAADF-STEM was utilised to gain further insight into alloy formation in the Ga$_2$O$_3$ samples. Fig. 12 shows HAADF images for the commercial Pd loaded catalysts. Since XRD shows the presence of the Pd$_2$Ga alloy, the d spacings shown in Fig. 12 are likely to correspond to Pd$_2$Ga. Due to the addition of ZnO, the lattice fringes were not identifiable for PdZn/Ga$_2$O$_3$-1, therefore d-spacing measurements were not taken.

HAADF-STEM images with corresponding EDX elemental mapping revealed further information on the nature of the nanoparticle in Pd/Ga$_2$O$_3$-2, Fig. 13. Pd and Ga EDX overlap, showing the presence of the alloy, and according to the lattice spacing of 0.27 and 0.23 nm, a Pd$_2$Ga alloy can be identified. The Pd$_2$Ga alloy is also supported by XRD where the (112), (210) and (202) planes are assigned at 35.8, 39.6, and 40.1°. From Ga EDX mapping, Ga$_2$O$_3$ is at the base of the nanoparticle, as seen from the oxygen EDX map, showing the interface of the Pd-Ga nanoparticle and the support. EDX mapping also confirms the infiltration of Ga into the Pd nanoparticle supporting the formation of the Pd-Ga alloy. However, the PdZn/Ga$_2$O$_3$ catalyst, Fig. 13, shows Zn associated with the Pd nanoparticles and not Ga, again confirming the preference for the

PdGaZn system to form the PdZn alloy rather than the Pd$_2$Ga alloy.

Fig. 14 shows the HAADF imaging with corresponding Pd, Zn, Ga and O EDX mapping for PdZn/Ga$_2$O$_3$-2. Pd metal clearly dominates in the nanoparticle with some association with Zn, likely corresponding to the PdZn alloy, as XPS also suggested. ZnO appears also to cover the Ga$_2$O$_3$ support, because at this ratio of Zn:Pd (~5:1) there is excess Zn above that required for PdZn alloy formation.

It appears that the PdZn alloy probably forms because of the CVI process where the Pd and Zn acacs are intimately mixed at the surface of the Ga$_2$O$_3$, combined with the difficulty of reducing the Ga oxide. This is then very different from the In$_2$O$_3$ case, where the Pd$_2$In$_3$ alloy dominates. As mentioned above the enthalpy of reduction for the two oxides is ~80 kJ/mol for In$_2$O$_3$ and 235 kJ/mol for Ga$_2$O$_3$, and presumably this is the main cause of the difference. In$_2$O$_3$ is so easily reduced that it can form the alloy even in the presence of Zn under the preparation conditions. Note that the enthalpy of reduction of ZnO is similar to that for In$_2$O$_3$, but much lower than that of Ga$_2$O$_3$. The presence of the Pd$_2$Ga alloy has a much more beneficial effect on the performance of the catalyst than the Pd$_2$In$_3$, presumably because the former is exposed to reactants, and hence enhances hydrogen supply, than does the latter which is coated in an indium oxide layer.

In terms of the mechanism of methanol synthesis, see Fig. 15, it is apparent that a crucial component is a reducible oxide. This plays the role of a redox agent, that is, it can oxidise the gas phase (thus forming oxygen vacancies) and can then be re-oxidised by gas phase CO$_2$ (and thus refilling the anion vacancies). The role of the metal is then to hydrogenate the intermediate on the oxide to the formate, which is identified by many authors as being the crucial intermediate to methanol production. However, Pd itself is too active, since it strongly adsorbs CO, and can dissociate it, resulting in both methane formation and CO
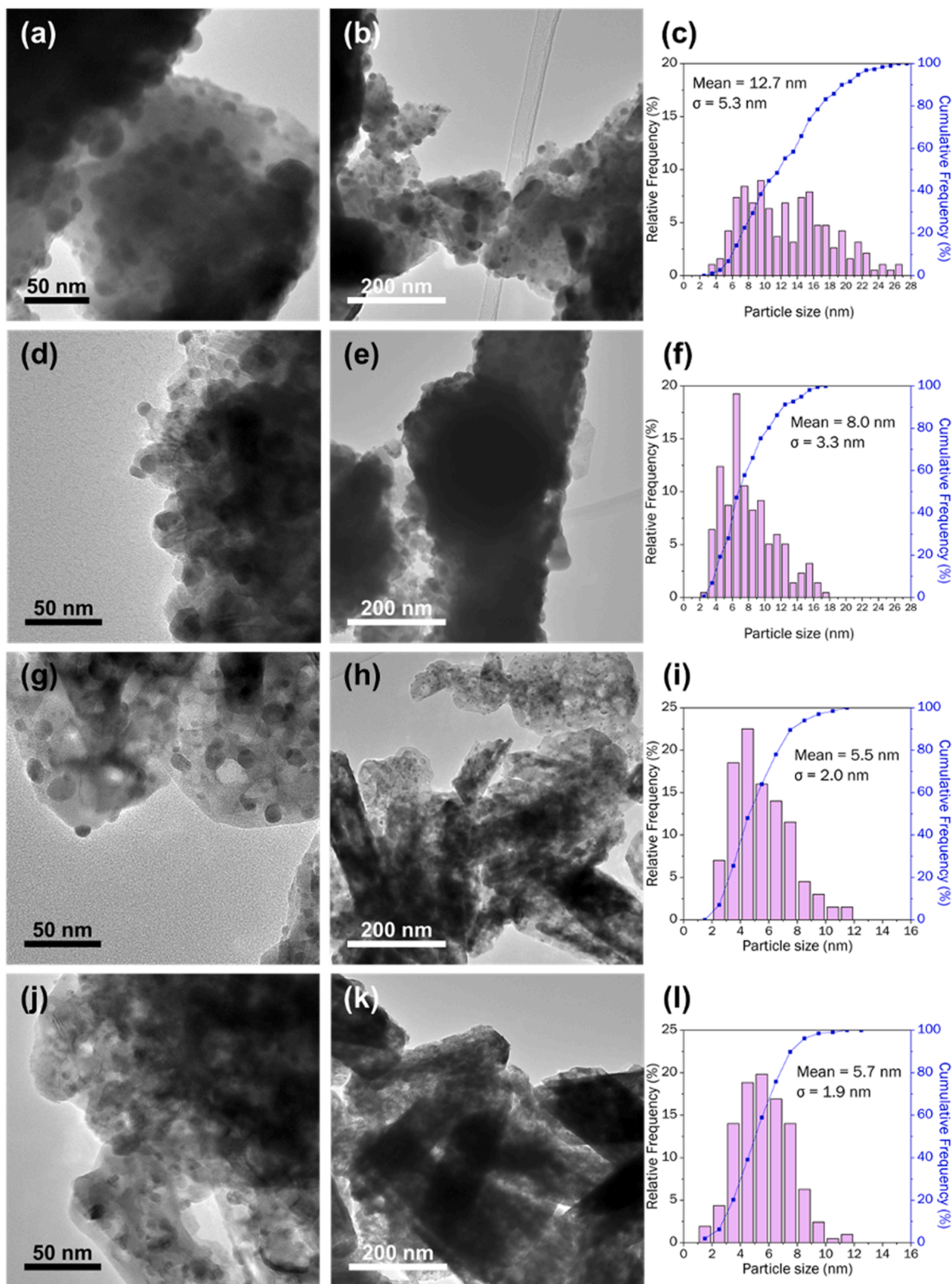
Fig. 10. Representative TEM images at 30 kx and 100 kx, and particle size distributions of Pd/Ga$_2$O$_3$-1 (a-c), PdZn/Ga$_2$O$_3$-1 (d-f), Pd/Ga$_2$O$_3$-2 (g-i), and PdZn/Ga$_2$O$_3$-2 (j-l). All catalysts were reduced at 400 °C for 1 h (5 °C min^{-1}) under 5 % H$_2$/Ar prior to analysis.
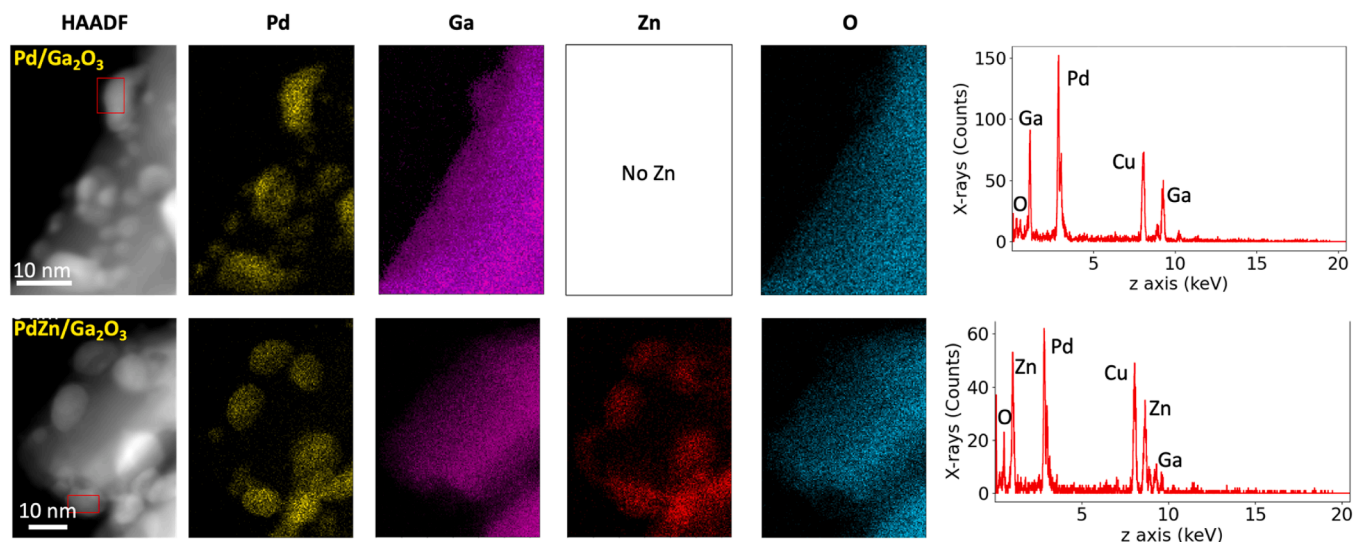
Fig. 11. STEM-EDX data demonstrating the alloying of nanoparticles after reduction at 400 °C for Pd/Ga_2O_3 (upper panels) and $PdZn/Ga_2O_3$ (lower panels). The EDX spectra (right) are taken from the red box indicated on the corresponding HAADF-STEM image. EDX maps are produced from a sum of all counts around the $K\alpha$ peak (for Ga, Zn and O) or the $L\alpha_1$ peak (for Pd).
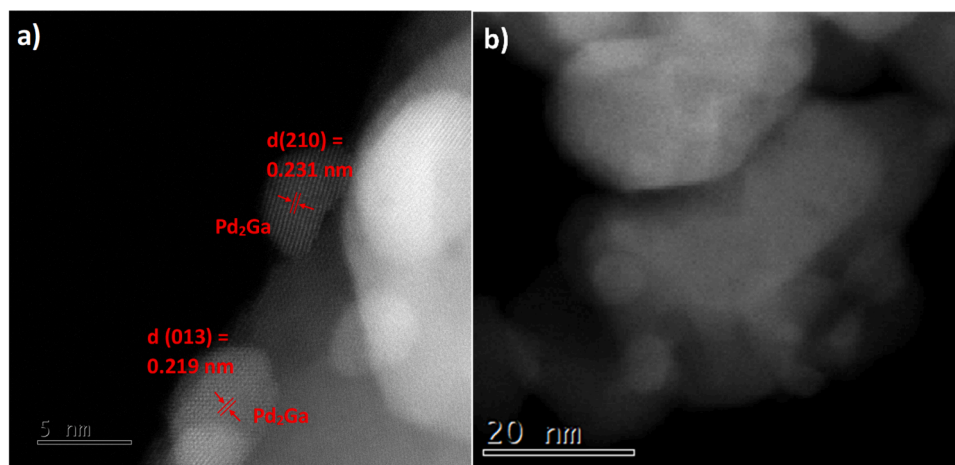
Fig. 12. Representative HAADF-STEM image for (a) Pd/Ga_2O_3-1 (b) $PdZn/Ga_2O_3$-1 after reduction at 400 °C, 1 h, 5 % H_2/Ar.

production [43, 69,70]. Pure Pd is mainly an agent for the reverse water gas shift reaction but produces significant amounts of methane too[70]. Alloying generally passivates the Pd to weaken the surface binding of adsorbed CO and to prevent its dissociation, while still permitting hydrogen dissociation. Indium oxide is a little different since, it appears to be able to do the hydrogen dissociation quite efficiently, and so go straight through to methanol. It is also different because when Pd is present, and notwithstanding that a PdIn alloy is produced after reduction, it plays little role in the reaction, because it becomes encapsulated by indium oxide.

4. Conclusions

In_2O_3 and Ga_2O_3-based catalysts were synthesised and investigated for CO_2 hydrogenation to methanol. In_2O_3 is a unique material as it can facilitate CO_2 and H_2 adsorption and activation without promoters and can produce methanol in high selectivity. There are some differences between catalysts prepared using synthesised and commercial materials, with the former having a much higher surface area than the latter. However, even though the synthesised material has much higher area, the activity is similar. Catalytic performance for the latter is improved a

little by adding 5 wt% Pd by CVI, whereas for the commercial catalyst it has relatively little effect. The high surface area of the synthesised oxide is lost when adding Pd and subsequent processing. When Zn is added both catalysts behave similarly, but the synthesised catalysts are slightly more active. XRD, XPS and TEM all clearly show the formation of the Pd_2In_3 alloy in the nanoparticles, but there is also considerable encapsulation of the metal nanoparticles by an oxide shell, probably In_2O_3. This explains why, overall, there is relatively little change in performance when the metal nanoparticles are present. It is to be noted also that the Pd_2In_3 alloy is favoured, even when Zn is added, in contrast to the Ga_2O_3 catalysts.

In contrast to In_2O_3, Ga_2O_3 has no activity under these conditions of synthesis and reaction. However, activity is significantly increased when Pd nanoparticles are present, and the catalyst is much more active than the equivalent In-based catalysts, with 3–4 times increased conversion. Analysis shows the formation of an alloy after reduction, the Pd_2Ga alloy, but in this case an oxide coating on the metal particles is not so evident. When Zn is added to the material, now the PdZn alloy is preferentially formed. There is an increase in conversion and selectivity for both the commercial and synthesised catalysts when Zn is added.
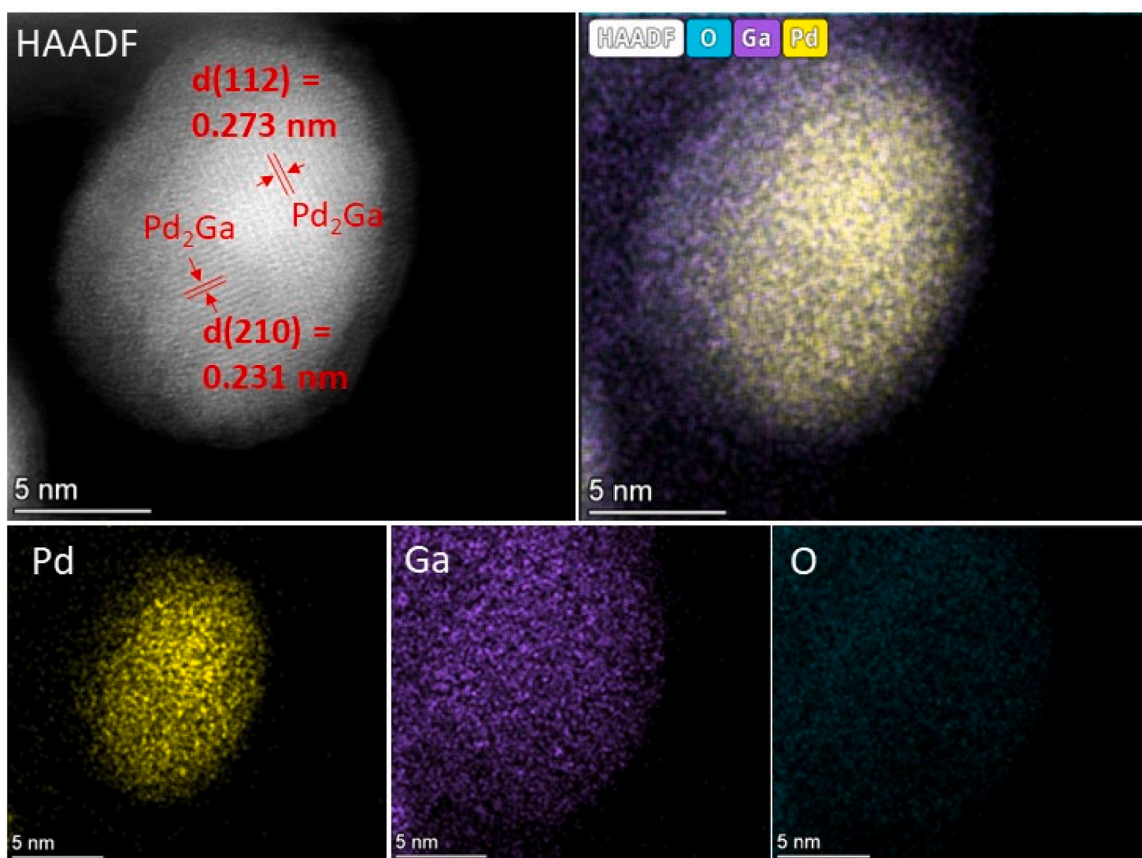
Fig. 13. Representative HAADF-STEM image and EDX elemental mappings of Pd, Ga and O signals and merged Pd +Ga + O signals for Pd/Ga$_2$O$_3$-2 after reduction (400 °C, 1 h, 5 % H$_2$/Ar).
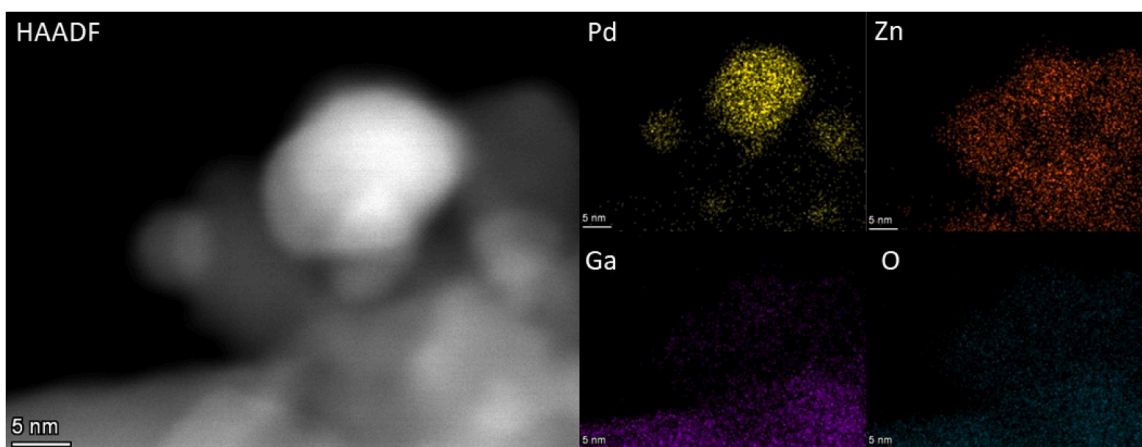

Fig. 14. Representative HAADF-STEM image and EDX elemental mappings of Pd, Zn, Ga and O signals PdZn/Ga$_2$O3–2 after reduction (400 °C, 1 h, 5 % H$_2$/Ar).

CRediT authorship contribution statement

Louise R. Smith: Supervision, Formal analysis, Data curation. **Oskar Wielgosz:** Data curation. **Isla E. Gow:** Writing – review & editing, Data curation. **Kieran J. Aggett:** Writing – review & editing, Formal analysis, Data curation. **David J. Morgan:** Funding acquisition, Data curation. **Thomas J. A. Slater:** Supervision, Funding acquisition. **Thomas E. Davies:** Writing – review & editing, Formal analysis, Data curation. **Nicholas F. Dummer:** Writing – review & editing, Supervision. **Samantha Fagan:** Data curation. **Stuart H Taylor:** Writing – review & editing, Investigation, Funding acquisition, Conceptualization. **Michael Bowker:** Writing – original draft, Supervision, Methodology, Investigation, Formal analysis, Conceptualization. **Graham J Hutchings:** Writing – review & editing, Supervision, Project administration, Investigation, Funding acquisition, Conceptualization. **Naomi Lawes:** Methodology, Investigation, Formal analysis, Data curation.

Declaration of Competing Interest

The authors declare the following financial interests/personal relationships which may be considered as potential competing interests. Michael Bowker reports financial support and article publishing charges
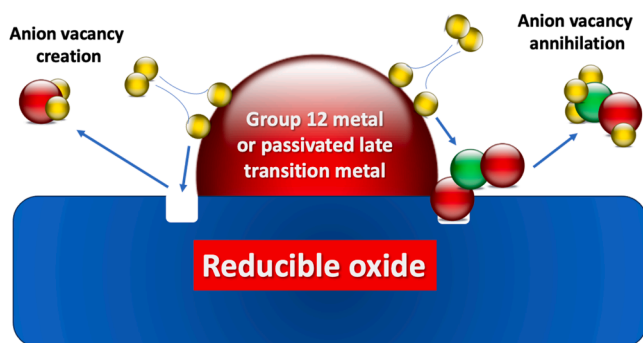
Fig. 15. Illustrating the overall mechanism of methanol synthesis on metal/oxide catalysts. These are a combination of a metal and reducible oxide. Cu is the commercial catalysts which is not capable of any C-O bond scission. Other late transition elements can be used, but only if in a passivated state (for example, as here, by alloy formation} which removes adjacent metal sites/ensembles which can dissociate the CO bond and make methane. The role of the metal is as a hydrogen dissociator to create anion vacancies in the oxide, which are then annihilated again by removal of an oxygen atom from CO2, which is then hydrogenated by spillover through to methanol. Yellow spheres – hydrogen, green – carbon, red – oxygen and the large red sphere is a nano-particle of the metal component.

Appendix A. Supporting information

Supplementary data associated with this article can be found in the online version at doi:10.1016/j.apcata.2024.119735.

References

[1] M.I. Malik, N. Abatzoglou, I.E. Achouri, Methanol to formaldehyde: an overview, Catalysts 11 (2021) 893.
[2] C. Brookes, M. Bowker, P.P. Wells, Catalysts for the selective oxidation of methanol, Catalysts 6 (2016) 92.
[3] G. Pacchioni, H.-J. Freund, Controlling the charge state of supported nanoparticles in catalysis, Chem. Soc. Rev. 47 (2018) 8474–8502.

[4] G. Malta, S.A. Kondrat, S.J. Freakley, C.J. Davies, L. Lu, S. Dawson, A. Thetford, E. K. Gibson, D.J. Morgan, W. Jones, P.P. Wells, P. Johnston, C.R.A. Catlow, C. J. Kiely, G.J. Hutchings, Identification of single-site gold catalysts in acetylene hydrochlorination, Science 355 (2017) 1399–1402.
[5] S. Penner, M. Armbruster, Steering the catalytic properties of intermetallic compounds and alloys, ChemCatChem 7 (2015) 374–392.
[6] H. Lorenz, C. Rameshan, T. Bielz, N. Memmel, W. Stadlmayr, L. Mayr, Q. Zhao, S. Soisuwan, B. Klotzer, S. Penner, From oxide supported Palladium to intermetallic Palladium phases, ChemCatChem 5 (2013) 1273–1285.
[7] J. Ye, Q. Ge, C. Liu, Effect of PdIn bimetallic particle formation on CO2 reduction over the Pd-In/SiO2 catalyst, Chem. Eng. Sci.. 135 (2015) 193–201.
[8] A. García-Trenco, A. Regoutz, E.R. White, D.J. Payne, M.S.P. Shaffer, C.K. Williams, PdIn intermetallic nanoparticles for the hydrogenation of CO2 to methanol, Appl. Catal. B Environ. 220 (2018) 9–18.
[9] N. Rui, Z. Wang, K. Sun, J. Ye, Q. Ge, C. Liu, CO2 Hydrogenation to methanol over Pd/In2O3: effects of Pd and oxygen vacancy, Appl. Catal. B Environ.. 218 (2017) 488–497.
[10] J. Ye, C. Liu, D. Mei, Q. Ge, Methanol synthesis from CO2 hydrogenation: combined DFT and kinetic study, J. Catal. 317 (2014) 44–53.
[11] N. Austin, B. Butina, G. Mpourmpakis, CO2 activation on bimetallic CuNi nanoparticles, Prog. Nat. Sci. Mater. Int 26 (2016) 487–492.
[12] F. Muttaqien, Y. Hamamoto, I. Hamada, K. Inagaki, Y. Shiozawa, K. Mukai, T. Koitaya, S. Yoshimoto, J. Yoshinobu, Y. Morikawa, CO2 adsorption on the copper surfaces: van der Waals density functional and TPD studies, J. Chem. Phys. 147 (2017) 094702.
[13] X. Liu, L. Sun, W.-Q. Deng, Theoretical Investigation of CO2 Adsorption and Dissociation on Low Index Surfaces of Transition Metals, J. Phys. Chem. C. 122 (2018) 8306–8314.
[14] M.S. Frei, C. Mondelli, J. Pérez-Ramírez, Development of In2O3-based catalysts for CO2-based methanol production, Chim. (Aarau) 74 (2020) 257–262.
[15] K. Li, J.G. Chen, CO2 hydrogenation to methanol over ZrO2-containing catalysts: insights into ZrO2 induced synergy, ACS Catal. 9 (2019) 7840–7861.
[16] M.S. Frei, C. Mondelli, A. Cesarini, F. Krumeich, R. Hauert, J.A. Stewart, D. Curulla Ferré, J. Pérez-Ramírez, Role of zirconia in indium oxide-catalyzed CO2 hydrogenation to methanol, ACS Catal. 10 (2020) 1133–1145.
[17] X. Nie, W. Li, X. Jiang, X. Guo, C. Song, Chapter two - recent advances in catalytic CO2 hydrogenation to alcohols and hydrocarbons, Adv. Catal. 65 (2019) 121–233.
[18] J. Wang, G. Zhang, J. Zhu, X. Zhang, F. Ding, A. Zhang, X. Guo, C. Song, CO2hydrogenation to methanol over In2O3-based catalysts, ACS Catal. 11 (2021) 1406–1423.
[19] D. Liu, W.W. Lei, B. Zou, S.D. Yu, J. Hao, K. Wang, B.B. Liu, Q.L. Cui, G.T. Zou, High-pressure x-ray diffraction and Raman spectra study of indium oxide, J. Appl. Phys. 104 (2008) 83506.
[20] J. Wang, C.-Y. Liu, T.P. Senftle, J. Zhu, G. Zhang, X. Guo, C. Song, Variation in the In2O3 crystal phase alters catalytic performance toward the reverse water gas shift reaction, ACS Catal. 10 (2020) 3264–3273.
[21] S. Dang, B. Qin, Y. Yang, H. Wang, J. Cai, Y. Han, S. Li, P. Gao, Y. Sun, Rationally designed indium oxide catalysts for CO2 hydrogenation to methanol with high activity and selectivity, Sci. Adv. 6 (2020) eaaz2060.
[22] T. Bielz, H. Lorenz, P. Amann, B. Klötzer, S. Penner, Water—gas shift and formaldehyde reforming activity determined by defect chemistry of polycrystalline In2O3, J. Phys. Chem. C. 115 (2011) 6622–6628.
[23] J. Ye, C. Liu, D. Mei, Q. Ge, Active oxygen vacancy site for methanol synthesis from CO2 hydrogenation on In2O3(110): a DFT study, ACS Catal. 3 (2013) 1296–1306.
[24] M.S.S. Frei, M. Capdevila-Cortada, R. García-Muelas, C. Mondelli, N. López, J.A. A. Stewart, D. Curulla Ferré, J. Pérez-Ramírez, Mechanism and microkinetics of methanol synthesis via CO2 hydrogenation on indium oxide, J. Catal. 361 (2018) 313–321.
[25] O. Martin, A.J. Martín, C. Mondelli, S. Mitchell, T.F. Segawa, R. Hauert, C. Drouilly, D. Curulla-Ferré, J. Pérez-Ramírez, Indium Oxide as a Superior Catalyst for Methanol Synthesis by CO2 Hydrogenation, Angew. Chem. Int. Ed. 55 (2016) 6261–6265.
[26] Z. Han, C. Tang, J. Wang, L. Li, C. Li, Atomically dispersed Ptn+ species as highly active sites in Pt/In2O3 catalysts for methanol synthesis from CO2 hydrogenation, J. Catal. 394 (2021) 236–244.
[27] J. Wang, K. Sun, X. Jia, C. Liu, CO2 hydrogenation to methanol over Rh/In2O3 catalyst, Catal. Today 365 (2021) 341–347.
[28] K. Sun, N. Rui, C. Shen, C.-J. Liu, Theoretical Study of Selective Hydrogenation of CO2 to Methanol over Pt4/In2O3 Model Catalyst, J. Phys. Chem. C. 125 (2021) 10926–10936.
[29] A. Sharma, M. Varshney, H. Saraswat, S. Chaudhary, J. Parkash, H.-J. Shin, K.-H. Chae, S.-O. Won, Nano-structured phases of gallium oxide (GaOOH, α-Ga2O3, β-Ga2O3, γ-Ga2O3, δ-Ga2O3, and ε-Ga2O3): fabrication, structural, and electronic structure investigations, Int. Nano Lett. 10 (2020) 71–79.
[30] V. Ghodsi, S. Jin, J.C. Byers, Y. Pan, P.V. Radovanovic, Anomalous photocatalytic activity of nanocrystalline γ-phase Ga2O3 enabled by long-lived defect trap states, J. Phys. Chem. C. 121 (2017) 9433–9441.
[31] M. Akatsuka, Y. Kawaguchi, R. Itoh, A. Ozawa, M. Yamamoto, T. Tanabe, T. Yoshida, Preparation of Ga2O3 photocatalyst highly active for CO2 reduction with water without cocatalyst, Appl. Catal. B Environ. 262 (2020) 118247.
[32] S.J. Pearton, J. Yang, P.H. Cary, F. Ren, J. Kim, M.J. Tadjer, M.A. Mastro, A review of Ga2O3 materials, processing, and devices Appl. Phys. Rev, Appl. Phys. Rev. 5 (2018) 011301.
[33] M. Saito, T. Fujitani, M. Takeuchi, T. Watanabe, Development of copper/zinc oxide-based multicomponent catalysts for methanol synthesis from carbon dioxide and hydrogen, Appl. Catal. A Gen. 138 (1996) 311–318.

[34] J. Toyir, P.R. de la Piscina, J.L.G. Fierro, N. Homs, Highly effective conversion of CO2 to methanol over supported and promoted copper-based catalysts: influence of support and promoter, Appl. Catal. B Environ. 29 (2001) 207–215.

[35] J. Toyir, P. Ramírez de la Piscina, J.L.G. Fierro, N. Homs, Catalytic performance for CO2 conversion, Catalytic performance for CO2 conversion to methanol of gallium-promoted copper-based catalysts: influence of metallic precursors, Appl. Catal. B Environ. 34 (2001) 255–266.

[36] S.E. Collins, J.J. Delgado, C. Mira, J.J. Calvino, S. Bernal, D.L. Chiavassa, M. A. Baltanás, A.L. Bonivardi, The role of Pd–Ga bimetallic particles in the bifunctional mechanism of selective methanol synthesis via CO2 hydrogenation on a Pd/Ga2O3 catalyst, J. Catal. 292 (2012) 90–98.

[37] T. Fujitani, M. Saito, Y. Kanai, T. Watanabe, J. Nakamura, T. Uchijima, T. Uchijima, Development of an active Ga2O3 supported palladium catalyst for the synthesis of methanol from carbon dioxide and hydrogen, Appl. Catal. A Gen. 125 (1995) L199–L202.

[38] R. Manrique, R. Jiménez, J. Rodríguez-Pereira, V.G. Baldovino-Medrano, A. Karelovic, Insights into the role of Zn and Ga in the hydrogenation of CO2 to methanol over Pd, Int. J. Hydrog. Energy 44 (2019) 16526–16536.

[39] R. Manrique, J. Rodríguez-Pereira, S.A. Rincón-Ortiz, J.J. Bravo-Suárez, V. G. Baldovino-Medrano, R. Jiménez, A. Karelovic, The nature of the active sites of Pd–Ga catalysts in the hydrogenation of CO2 to methanol, Catal. Sci. Technol. 10 (2020) 6644–6658.

[40] S.E. Collins, M.A. Baltanás, J.J. Delgado, A. Borgna, A.L. Bonivardi, CO2 hydrogenation to methanol on Ga2O3-Pd/SiO2 catalysts: dual oxide-metal sites or (bi)metallic surface sites? Catal. Today 381 (2021) 154–162.

[41] X. Liu, Q. Gu, Y. Zhang, X. Xu, H. Wang, Z. Sun, L. Cao, Q. Sun, L. Xu, L. Wang, S. Li, S. Wei, B. Yang, J. Lu, Atomically thick oxide overcoating stimulates low-temperature reactive metal–support interactions for enhanced catalysis, J. Am. Chem. Soc. 145 (2023) 6702–6709.

[42] H. Farag, Z.M. Hanafi, M. Dawy, E.L. El Aziz, Characterization of ZnO nanopowders synthesized by the direct precipitation method, Can. J. Pure Appl. Sci. 4 (2010) 1303–1309.

[43] M. Bowker, N. Lawes, I. Gow, J. Hayward, J.R. Esquius, N. Richards, L.R. Smith, T. J.A. Slater, T.E. Davies, N.F. Dummer, L. Kabalan, A. Logsdail, R.C. Catlow, S. Taylor, G.J. Hutchings, The critical role of βPdZn alloy in Pd/ZnO catalysts for the hydrogenation of carbon dioxide to methanol, ACS Catal. 12 (2022) 5371–5379.

[44] N. Fairley, V. Fernandez, M. Richard-Plouet, C. Guillot-Deudon, J. Walton, E. Smith, D. Flahaut, M. Greiner, M. Biesinger, S. Tougaard, D. Morgan, J. Baltrusaitis, Systematic and collaborative approach to problem solving using X-ray photoelectron spectroscopy, Appl. Surf. Sci. Adv. 5 (2021) 100112.

[45] F. Shi, H. Qiao, Preparations, properties and applications of gallium oxide nanomaterials – a review, Nano Sel. 3 (2022) 348–373.

[46] C.F. Holder, R.E. Schaak, Tutorial on powder X-ray diffraction for characterizing nanoscale materials, ACS Nano 13 (2019) 7359–7365.

[47] H. Bahruji, M. Bowker, G. Hutchings, N. Dimitratos, P. Wells, E. Gibson, W. Jones, C. Brookes, D.J. Morgan, G. Lalev, Pd/ZnO catalysts for direct CO2 hydrogenation to methanol, J. Catal. 343 (2016) 133–146.

[48] H. Bahruji, M. Bowker, W. Jones, J. Hayward, J. Ruiz Esquius, D.J. Morgan, G. J. Hutchings, PdZn catalysts for CO2 hydrogenation to methanol using chemical vapour impregnation (CVI), Faraday Discuss. 197 (2017) 309.

[49] Carlos Quilis, Noelia Mota, Barbara Pawelec, Elena Millan, Rufino M. Navarro Yerga, Intermetallic PdZn/TiO2 catalysts for methanol production from CO2 hydrogenation: The effect of ZnO loading on PdZn-ZnO sites and its influence on activity, Appl. Catal. B Environ. 321 (2023) 122064.

[50] Y. Wang, D. Wu, T. Liu, G. Liu, X. Hong, Fabrication of PdZn alloy catalysts supported on ZnFe composite oxide for CO2 hydrogenation to methanol, J. Colloid Interface Sci. 597 (2021) 260–268.

[51] I. Mashkovsky, P. Markov, G. Bragina, G. Baeva, A. Rassolov, I. Yakushev, M. Vargaftik, A. Stakheev, Highly-ordered PdIn intermetallic nanostructures obtained from heterobimetallic acetate complex: formation and catalytic properties in diphenylacetylene hydrogenation, Nanomaterials 8 (2018) 769.

[52] I.R. Harris, M. Norman, A.W. Bryant, A study of some Pd-In alloys, J. Less Common Met. 16 (1968) 427–440.

[53] J.L. Snider, V. Streibel, M.A. Hubert, T.S. Choksi, E. Valle, D.C. Upham, J. Schumann, M.S. Duyar, A. Gallo, F. Abild-Pedersen, T.F. Jaramillo, Revealing the synergy between oxide and alloy phases, ACS Catal. 9 (2019) 3399–3412.

[54] M.S. Frei, C. Mondelli, R. García-Muelas, K.S. Kley, B. Puértolas, N. López, O. V. Safonova, J.A. Stewart, D. Curulla Ferré, J. Pérez-Ramírez, Atomic-scale engineering of indium oxide promotion by palladium for methanol production via CO2 hydrogenation, Nat. Commun. 10 (2019) 3377.

[55] J. Zhong, X. Yang, Z. Wu, B. Liang, Y. Huang, T. Zhang, Chem. Soc. Rev. 49 (2020) 1385.

[56] W.-J. Shen, K.-W. Jun, H.-S. Choi, K.-W. Lee, Thermodynamic Investigation of Methanol and Dimethyl Ether Synthesis from CO2 Hydrogenation, Korean J. Chem. Eng. 17 (2000) 210–216.

[57] S. Furukawa, M. Endo, T. Komatsu, Bifunctional catalytic system effective for oxidative dehydrogenation of 1-Butene and n-Butane using Pd-based intermetallic compounds, ACS Catal. 4 (2014) 3533–3542.

[58] T. Skála, K. Veltruská, M. Moroseac, I. Matoli, G. Korotchenkov, V. Matoli, Study of Pd–In interaction during Pd deposition on pyrolytically prepared In2O3, Appl. Surf. Sci. 205 (2003) 196–205.

[59] M. Armbrüster, R. Schlögl, Y. Grin, Intermetallic compounds in heterogeneous catalysis, Sci. Technol. Adv. Mater. 15 (2014) 034803.

[60] C. Rameshan, W. Stadlmayr, S. Penner, H. Lorenz, L. Mayr, M. Hävecker, R. Blume, T. Rocha, D. Teschner, A. Knop-Gericke, R. Schlögl, D. Zemlyanov, N. Memmel, B. Klötzer, In situ XPS study of methanol reforming on PdGa near-surface intermetallic phases, J. Catal. 290 (2012) 126–137.

[61] J. Osswald, R. Giedigkeit, R. Jentoft, M. Armbruster, F. Girgsdies, K. Kovnir, T. Ressler, Y. Grin, R. Schlogl, Palladium Gallium intermetallic compounds for the selective Hydrogenation of acetylene, J. Catal. 258 (2008) 210–218.

[62] Z. Ryżyńska, P. Wiśniewski, D. Kaczorowski, W. Xie, R.J. Cava, T. Klimczuk, M. J. Winiarski, Superconductivity in the endohedral Ga cluster compound PdGa5, J. Phys. Chem. C 125 (2021) 11294–11299.

[63] J. Cored, C.W. Lopes, L. Liu, J. Soriano, G. Agostini, B. Solsona, R. Sánchez-Tovar, P. Concepción, Cu-Ga3+-doped wurtzite ZnO interface as driving force for enhanced methanol production in co-precipitated Cu/ZnO/Ga2O3 catalysts, J. Catal. 407 (2022) 149–161, https://doi.org/10.1016/j.jcat.2022.01.032.

[64] X. Liu, M. Wang, C. Zhou, W. Zhou, K. Cheng, J. Kang, Q. Zhang, W. Deng, Y. Wang, Selective transformation of carbon dioxide into lower olefins with a bifunctional catalyst composed of ZnGa2O4 and SAPO-34, Chem. Commun. 54 (2018) 140–143.

[65] M.M.-J.J. Li, Z. Zeng, F. Liao, X. Hong, S.C.E. Tsang, Enhanced CO2 Hydrogenation to Methanol over CuZn Nanoalloy in Ga Modified Cu/ZnO Catalysts, J. Catal. 343 (2016) 157–167.

[66] O. Oyola-Rivera, M.A. Baltanás, N. Cardona-Martínez, CO2 hydrogenation to methanol and dimethyl ether by Pd–Pd2Ga catalysts supported over Ga2O3 polymorp, J. CO2 Util. 9 (2015) 8–15.

[67] L. Li, B. Zhang, E. Kunkes, K. Föttinger, M. Armbrüster, D.S. Su, W. Wei, R. Schlögl, M. Behrens, Ga-Pd/Ga2O3 catalysts: the role of Gallia Polymorphs, intermetallic compounds, and pretreatment conditions on selectivity and stability in different reactions, ChemCatChem 4 (2012) 1764–1775.

[68] C.A. Schneider, W.S. Rasband, K.W. Eliceiri, NIH Image to ImageJ: 25 years of image analysis, Nat. Methods 9 (2012) 671–675.

[69] N. Lawes, et al., Methanol synthesis from CO2 and H2 using supported Pd alloy catalysts, Faraday Discuss. 242 (2023) 193.

[70] N. Lawes, K.J. Aggett, L.R. Smith, T.J.A. Slater, M. Dearg, D.J. Morgan, N. F. Dummer, S.H. Taylor, G.J. Hutching, M. Bowker, Zn Loading effects on the selectivity of PdZn catalysts for CO2 hydrogenation to methanol, Catal. Lett. 154 (2024) 1603–1610.